Investigation on Entropy Signature of Objects

By

Adam D'Silva

Submitted to the graduate degree program in Aerospace Engineering and Graduate Faculty of the University of Kansas in partial fulfillment of the requirements for the degree of Master of Science.

_____

Chairperson: Dr. S. Farokhi

_____

Dr. R. Taghavi

_____

Dr. S. Keshmiri

Date Defended: January 27th, 2017

THE UNIVERSITY OF KANSAS

The Thesis Committee of Adam D'Silva certifies that this is the approved version of the following thesis:

Investigation on Entropy Signature of Objects

_____

Chairperson: Dr. S. Farokhi

_____

Dr. R. Taghavi

_____

Dr. S. Keshmiri

Date Defended: January 27th, 2017

Abstract

With the use of modern configuration and advanced stealth technologies, aircraft have the ability to minimize their signatures significantly. The three main signatures being infrared, radar, and noise. A new observable, not taken into consideration, is entropy trail. This is a new and exciting area of research, to detect an object in motion, based on its entropy trail. The objective is to investigate two objects, a sphere and wing, generate an entropy trail regardless of shape, size, or implemented low observable technologies. Literature review established that the sphere and wing had negligible IR, radar, and noise signatures. IR signature was 0.18% and 0.07% off ambient temperature, radar signature was -19.9 dBm^2 and -10.6dBm^2, and noise signature was negligible since the incoming flow was M $\leq$ 0.1. The entropy trail of a sphere and wing were investigated using the 2nd Law of Thermodynamics and Gibbs equation. The trails were determined with CFD analysis at non-dimensionalized distances, away from the trailing edge, of the models. Wind tunnel measurements validated CFD results by measuring total pressure at arbitrary positions in the wake. Temperature measurements were not considered since the process is adiabatic. The results were in agreement between CFD and wind tunnel expect for the wing at 16 degrees angle of attack. This was due to the presence of a vortex and separated flow, which is difficult to capture with pitot tubes.

Table of Contents

List of Figures

List of Tables

List of Symbols

Symbol	Description	Units
A	Area	m^2
b	Span	m, in
c	Chord	m
C_d	Coefficient of Drag	~
C_l	Coefficient of Lift	~
c_p	Specific Heat at Constant Pressure	J/kg-K
D	Diameter	m, in
E	Electric Field	V/m
E	Internal Energy	J
E	Irradiance	W/m^2
f	Elliptic Relaxation Function	~
H	Enthalpy	J

H .... Magnetic Field .... A/m

I ....Radiant Intensity .... W/sr

k ....Turbulent Kinetic Energy per unit Mass...J/kg

L.. Radiance .... W/m-sr

M... Mach number .... ~

P..Pressure .... Pa

Q .... Heat Exchange ....J

R .... Range.. m

R ....Gas Constant.. J/kg-K

Re......................................Reynolds Number .... ~

S .... Entropy .... J/kg-K

T.. Temperature .... K, F

v ....Velocity.. m/s, mph

V .... Voltage .... mV, V

� .... Volume ....m^3

W ....Work done.. W

Δ.. Change.. ~

ρ.. Density ....kg/m^3

Ω...Solid Angle .... sr

Λ ....Sweep Angle .... deg

σ .... Radar Cross Section ....m^2, dBm^2

ø .... Diameter .... m, in

ω .... Specific Dissipation 1/s

ε ....Turbulent Dissipation ....J/kg-s

υ.. Wall-normal Velocity Fluctuation .... ~

Subscript　　　　　　　　　**Description**

D ....Diameter

L.E. .... Leading Edge

R .... Receiver

Ref .... Reference

s..Source

t.. Total

0 .... Ambient

2 .... Arbitrary point in the wake of the model

Acronym	**Description**
AOA	Angle of Attack
CBT	Center Body Tailpipe
CFD	Computational Fluid Dynamics
EM	Electromagnetic
IR	Infrared
IRSL	Infrared Signature Level
LES	Large Eddy Simulation
PEC	Perfect Electric Conductor
RAM	Radar Absorbing Material
RANS	Reynolds-Averaged Navier-Stokes
RCS	Radar Cross Section

1   <u>Introduction</u>

The idea of investigating entropy signatures, as a new observable, stemmed off an abstract by Dr. Farokhi, Dr. Taghavi, and Dr. Keshmiri [Ref. 1]. This is a new and exciting area of research. The motivation is, due to advanced stealth technologies and configurations, aircraft are capable of minimizing detection. The primary forms of detection are radar, infrared or thermal, and noise signatures. Radar stealth technologies utilize advanced configuration designs, carbon composites, and radar-absorbing materials to reduce aircraft detection range. Noise suppression involves integration of quiet and calm jets into vehicles, and modified chevron nozzles. To reduce thermal signatures, blended rectangular nozzles, which are shielded from the ground, reduce the thermal intensity of an aircraft. Using the 2nd Law of Thermodynamics, any object in motion generates a unique entropy trail which once measured can be detected [Ref. 2 - 6]. The objective is, by using low observable technologies to minimize signatures, an aircraft can be detected based on its entropy trail or wake. Characterization of entropy wake is based on pressure and temperature disturbances.

Entropy wake of a sphere and wing, in motion, are investigated. Measurements are recorded, in the wake, at non-dimensional distances downstream of the models. Computational Fluid Dynamics (CFD) and wind tunnel measurements are conducted at a Reynolds number, based on diameter and chord, of 25700 and 20100 for the wing and sphere respectively. Since the direct measurement of entropy is difficult, the derived properties are measured. Gibbs equation is used to determine entropy, where the measurement of total pressure and temperature in the wake characterizes the objects entropy signature. Validation of CFD results is conducted via wind tunnel measurements at arbitrary locations in the objects wake.

2   Literature Review

Characterization of the three signatures, infrared, radar, and noise are discussed in this section. In addition, since the area of research is new, there is no published data on utilizing entropy signature to detect objects in motion. Therefore, recent and current research on entropy measurements will be presented.

2.1 Infrared Signature

Infrared (IR) was discovered by Sir William Herschel in 1800 through a series of experiments with a prism and mercury thermometers as sensors. He proved that light and IR have the same optical properties. IR is electromagnetic radiation, which travels at the speed of light in a vacuum and at slower speeds in other mediums; like air or glass [Ref. 7]. Figure 2.1 shows where IR is located in the electromagnetic spectrum.
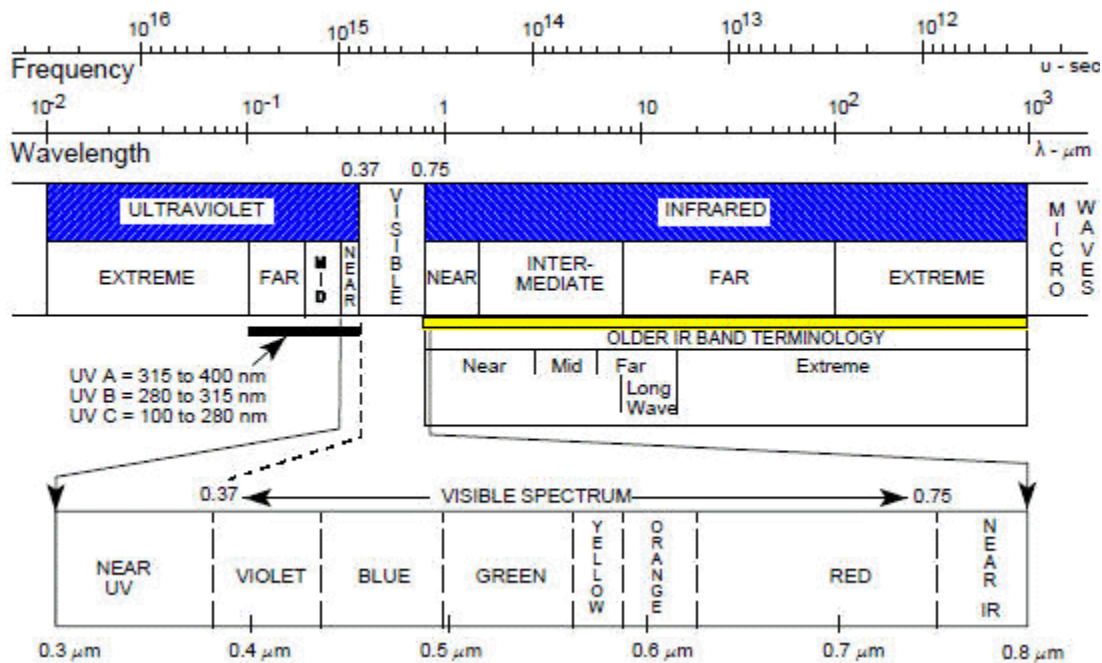
Figure 2.1: Electromagnetic Spectrum [Ref. 8]

Plank's law is necessary to understand aircraft IR signature, which is illustrated in Figure 2.2. The curves show the direct emissions from an object at different temperatures. It is observed that as the temperature increases the radiant emittance power increases at every wavelength [Ref. 7].
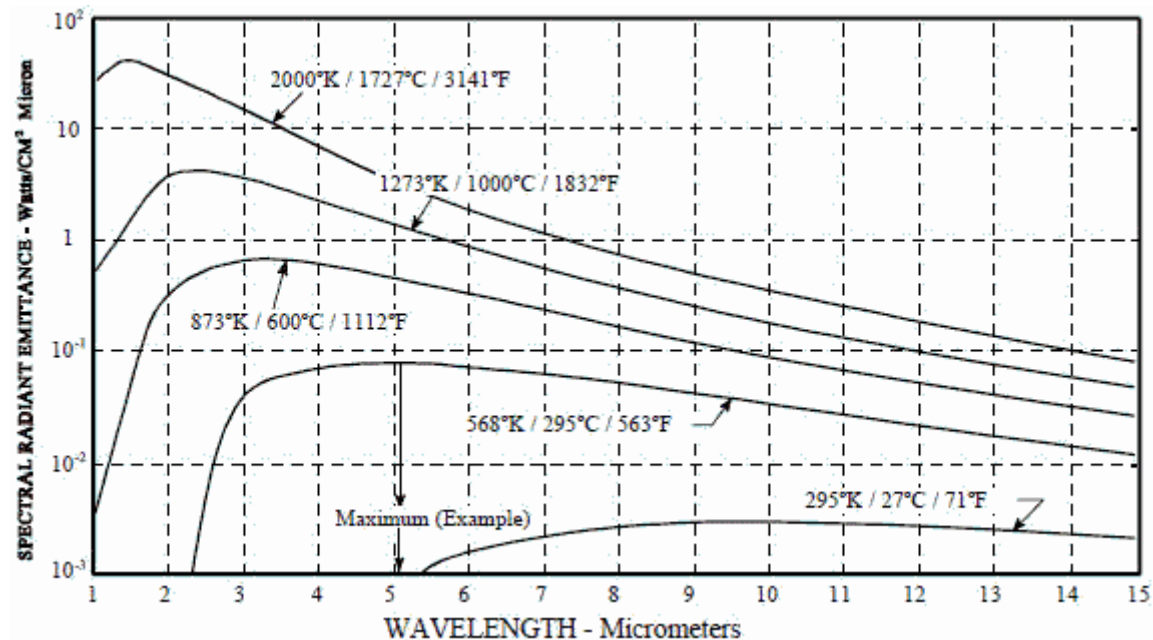
Figure 2.2: Spectral Radiant Emittance based on Plank's Law [Ref. 8]

IR signature detection of an aircraft is determined by the total thermal emissions and reflections. Figure 2.3 is an IR image of a low flying fighter jet and it is observed that the main IR emission is the exhaust plume.

Figure 2.3: IR Image of a Low Flying Fighter Jet [Ref 9]

The total detectable IR is the sum of the components that radiate [Ref. 7 and 10] which include, the airframe (which include solar and terrestrial reflections), aerodynamically heated skin due to friction, engine hot parts consisting of the aft turbine face, engine core, and interior nozzle sidewalls. The intensity of the radiation from an aircraft is non-uniform and it depends on the aspect angle. Figure 2.4 illustrates

12

the IR signature intensity based on aspect angle for a helicopter. It is observed that the selection of the aspect angle determines the intensity of the aircraft's IR signature.

Figure 2.4: IR Signature Range Based on Aspect Angle of a Helicopter [Ref 5]

The main components with high IR intensity is engine hot parts, engine plume, and airframe [Ref. 7 and 10]. Engine hot parts refers to any surface heated to a high temperature by the exhaust plume. The turbine face component has the highest temperature that appears as a bright high-radiance ring, where the center of the ring has a low radiance. According to Planck's Law, hot solid materials have a spectral distribution where engine hot 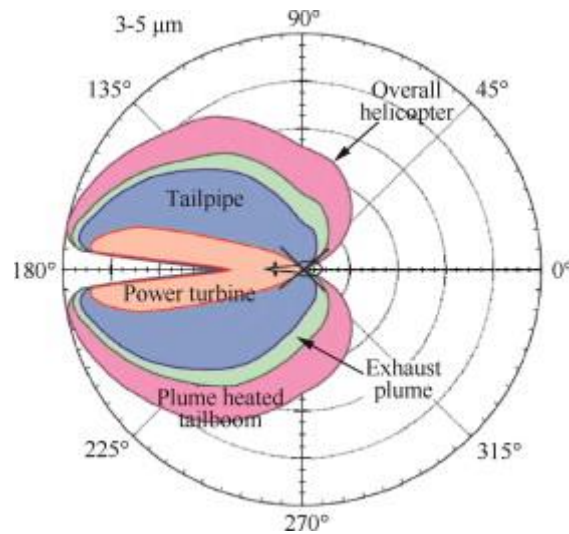parts range from 450 to 700 C [Ref. 7 and 10]. Exhaust plumes consist of gases such as CO_2, CO, NOx, and H_2O (vapor) where CO_2 is the most important contributor to IR-radiation signature [Ref. 12]. The greatest radiance is at the exit of the nozzle and then diminishes with distance due to the exhaust gases being cooled by mixing with air [Ref. 7].

Airframe have two signatures, absolute and contrast. Absolute is the target signature without any background radiation. Contrast is the difference between absolute target and absolute background radiance. Contrast varies based on the background conditions, the higher the background conditions the lower the contrast conditions are and vice versa. Factors that affect contrast signatures are background radiance level, airframe temperature and emissivity, and solar and terrestrial illumination. Equation (2.1) is a general estimation for airframe temperature [Ref. 7].

$$T_R = T_0(1 + 0.17M^2) \tag{2.1}$$

Where 'T_R' is the recovery temperature, 'T_0' is the ambient temperature, and 'M' is the Mach number.

Aircraft utilize stealth technologies to minimize signatures from components like hot engine parts and exhaust plumes [Ref. 13]. The YAH-64 helicopter implements the Black Hole Ocarina System, which reduces IR signature from metal parts by 30% and plume by 40%. The system directs the exhaust through special ducts, which combine the efflux with the air stream passing over the aircraft. This dissipates the plume to enhance the mixing process [Ref. 11 and 12]. Another system is the Center Body Tailpipe (CBT),

13

designed by Thompson et al. [Ref. 15]. It consists of a film cooled outer duct surrounded by a diffuser [Ref. 16 and 17]. To reduce exhaust plume intensity, the use of non-axisymmetric nozzles enhances the mixing of hot exhaust gases with ambient air. According to a study [Ref. 18], using a 60 degree notched nozzle can reduce the hottest magnitude length of the plume by 33%. Other ways to enhance mixing is to redesign the nozzle exit by using turbulators, chevrons, lobes, scalloped edges, and corrugated surfaces [Ref. 10].

Suppression of airframe IR magnitude is based on stealth technology that mask or reduce the emissivity of aircraft skin due to the environment. Heat pipe cooling, liquid evaporative cooling, and thermocouples use systems that sense the background temperature and heat/cool the skin accordingly, resulting in IR camouflage. The skin is heated/cooled using a thermoelectric module that converts electrical energy into a temperature gradient, which is varied by the applied voltage [Ref. 10]. Reduction in emissivity of radiating surface is through altering the surface physical and chemical properties. One method to alter the physical property is by coating/painting the surface with material that has a lower emissivity. Specific materials for low IR emissivity are explained in reference 14 and 19. Other methods involve using multiple cavities [Ref. 20], or a three-color camouflage system that adopts the color of the natural background [Ref. 21].

2.2 <u>Radar Signature</u>

Radar cross section (RCS) is an estimate of observability of a target, depending on its external features and electromagnetic (EM) properties, when impinged by a radar wave. The interaction between the target and radar wave results in part of the energy being absorbed and the remaining reflected or diffracted. The reflected energy, known as scattering, can be measured in two ways. The first method is monostatic conditions, where the EM waves reflected by the target are measured in the same direction as the emitting source. The second type of measurement is bistatic condition, where the reflected waves are detected at a distance away from the transmitter [Ref. 22]. For an aircraft the total RCS is the summation of contributing components to the scattering of the radar wave. This includes diffraction at sharp edges, corners, multiple scattering, surface waves, etc. [Ref. 23] and the scattering intensity is based on aspect angle. Starting at the nose-on angle and moving away, the wing edge becomes the major contributor to the overall RCS. At an aspect angle of ±180 degrees, the major contributor to the overall RCS is the engine exhaust [Ref. 23]. Figure 2.5 demonstrations a variation in RCS with respect to the aspect angle of a C-29. The RCS exhibits a high peak at ±90 degrees, which is due to the wing and fuselage [Ref. 24].
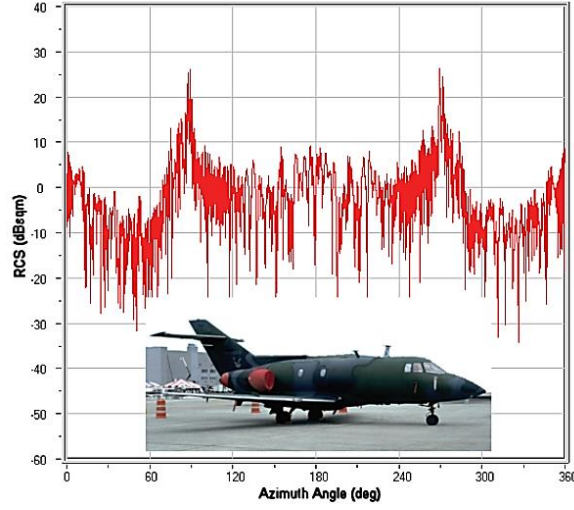
Figure 2.5: C-29 RCS Variation vs Aspect Angle [Ref 24]

Additional components to RCS are sensors and antennas mounted on the aircraft, this is known as antenna mode scattering [Ref. 25]. RCS is defined based on equation (2.2) [Ref. 22].

$$\sigma = 4\pi \lim_{R \to \infty} R^2 \frac{|E^S|^2}{|E^I|^2} = 4\pi \lim_{R \to \infty} R^2 \frac{|H^S|^2}{|H^I|^2} \tag{2.2}$$

Where 'σ' is the RCS of the target, 'E^S' is the reflected or scattered electric field, 'H^S' is the reflected or scattered magnetic field, 'E^I' is the incident electric field, and 'H^I' is the incident magnetic field. RCS is expressed in dBm^2 and equation (2.3) [Ref. 26] converts from m^2 to dBm^2.

$$\sigma(dBm^2) = 10\log_{10}[\sigma(m^2)] \tag{2.3}$$

Reducing the radar cross-section (RCS), radar-absorbing materials (RAMs) [Ref. 23], and passive and active cancellation [Ref. 27 and 28] increases an aircraft's stealth capabilities. For RCS reduction, shaping orients the surfaces and edges so that it reflects or diffracts the scattered energy away from the receiver. Figure 2.6, [Ref. 28], illustrates the effect of shaping of several shapes against a sphere (which is the uppermost curve). Out of the six shapes, the ogive exhibits the lowest RCS.
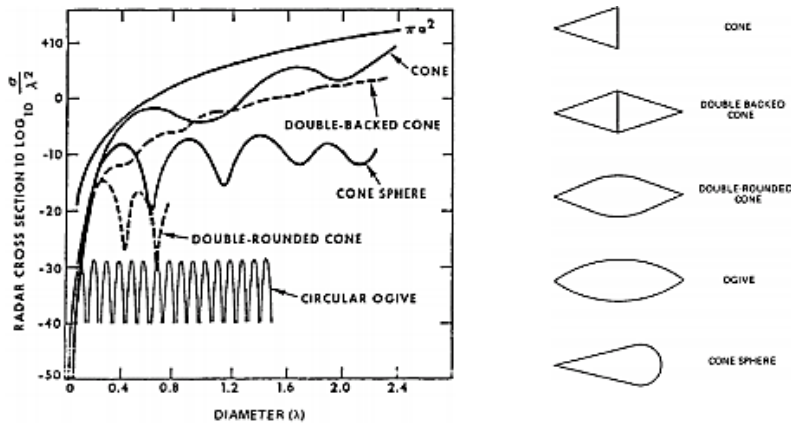

Figure 2.6: Effects of Shaping Cone on RCS [Ref. 28]

15

It is challenging to tailor every surface, to reduce the RCS intensity, at each aspect angle. Eventually a surface will see a normal incidence at which the echoed wave magnitude is high. The major aspect to shaping is utilizing angular or curved surfaces in areas that low RCS is not as important [Ref. 27 and 28]. Two examples of aircraft, Figure 2.7, that utilized shaping is the Northrop B-2 (right) and Lockheed F-117A (left).

Figure 2.7: F-117A (left) and B-2 (right) [Ref 29]

The F-117A uses surface faceting where edges are parallel so that majority of edge effects are collectively directed away from important viewing angles. B-2 uses faceting on the trailing edges of the wing [Ref. 30]. Figure 2.8 compares RCS of various objects [Ref. 24].
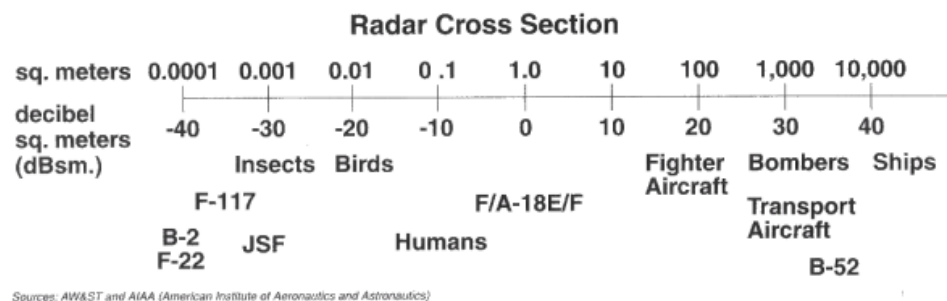

Figure 2.8: RCS of Various Objects [Ref. 24]

Radar-absorbing materials (RAM) reduce the energy reflected back to the radar by means of absorption through one or more loss mechanisms. This involves dielectric or magnetic properties of the material. The loss is the conversion of radio frequency energy into heat, and most absorbers do not dissipate enough energy to become detectably warm [Ref 27 and 28]. Simulations on RAM coated plates [Ref. 27], one made of perfect electric conductor (PEC) and the other graphite, exhibited RCS reduction. The dimensions of the plate specimen is 3 m × 2 m, in the 'x' and 'y' direction respectively, and the incident wave direction travels along the z-axis. The model rotates about the x-axis (theta) which is considered the aspect plane. Figure 2.9 displays the change in RCS based on aspect angle with and without RAM on the plates. It is observed that at 0 degrees there is an 87.7% reduction in RCS for the PEC plate

and a 93.2% reduction in RCS for graphite plate. The aspect angle from 0 to 60 degrees is displayed because it had the highest reduction in RCS.
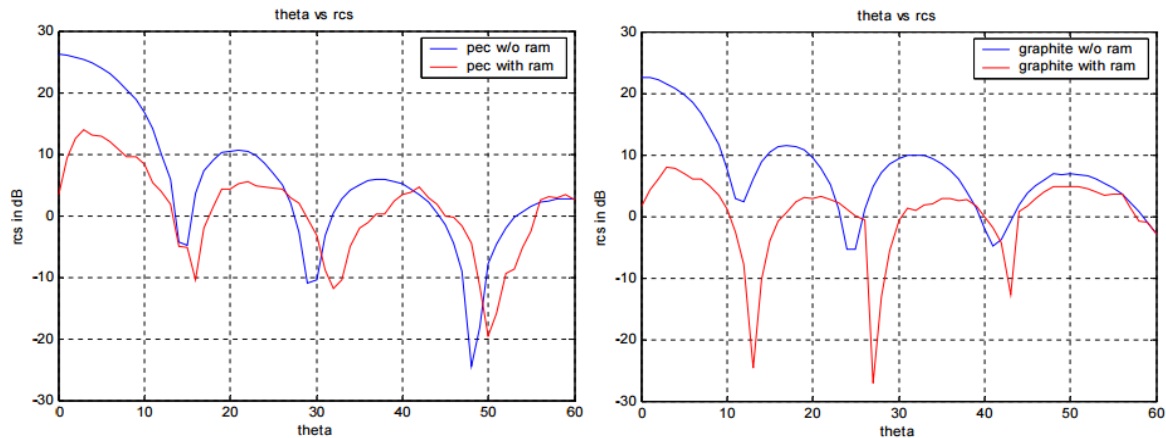

Figure 2.9: Comparison of using RAM on two plates. PEC (left) and Graphite (right) [Ref. 27]

In passive cancellation of RCS, a secondary echo source is introduced such that the amplitude and phase can be adjusted to cancel the primary source. This method is only effective for a narrow frequency band and is usually limited to a small spatial sector. It is also difficult to generate the required frequency dependence for this built-in impedance, and the reduction obtained for one frequency rapidly disappears as the frequency changes [Ref. 27 and 28].

For active cancellation of RCS, or active loading, the target transmits a signal that mimics the echo, which the radar will receive (but one-half wavelength out of phase). This cancels out the wave resulting in the radar receiver seeing no return. This method is very challenging because it requires fast processing. If poorly executed it could make the target more, rather than less, visible to the receiver [Ref. 28.]. In other words, it will act as a beacon [Ref. 31].

2.3 <u>Noise Signature</u>

Noise signature of an aircraft is aerodynamic noise from its vortices, wings, rotors, propellers, and engines. Each components noise intensity varies based on aircraft operation; take-off, cruise, and landing. The intensity of noise is directly proportional to the wing loading and speed [Ref. 23].

Liners consisting of classical honeycomb structure, with an outer plate that is porous or perforated, is one method to suppress nacelle noise. These liners act as Helmholtz resonators, allowing noise reduction at a certain range frequency. These liners are typically located near the fan of an engine. Another method treats the inlet lip with absorbers. This is efficient, but very ambitious, since the inlet lip uses de-icing techniques. Adding noise suppression techniques can be challenging since the two techniques are not necessarily compatible [Ref. 32].

Fan noise reduction also uses liners and lip treatment, but there are technologies specific to the fan component. The fan, a rotating part, generates two kinds of noise; self-noise and interaction noise that are

17

dependent on rotation speed [Ref. 33]. One method to reduce fan noise is to optimize the shape of the blade. An experiment, on two fan blade designs [Ref. 34], illustrate how optimizing the blade design reduces the baseline noise level. As observed in Figure 2.10, there is a significant noise reduction between the baseline and optimized blade design.
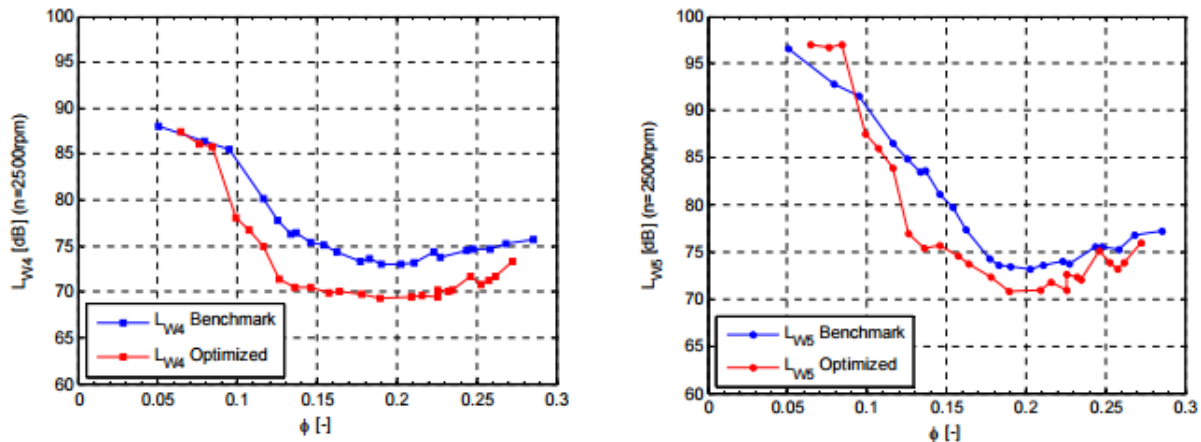

Figure 2.10: Acoustic Comparison of Benchmark and Optimized Fan. Left: sound power level in the room (suction side), Right: sound power level downstream of the duct (pressure side) [Ref. 34]

A second method targets fan tip Mach number reduction. This is crucial because for large fans the tip of the blade become transonic. It is resolved by using a gearbox. The use of Distributed Aft Fan Liners (DAFL) in the secondary duct have shown to reduce broadband noise by 5 dB and almost eliminates blade passing frequency tonal noise [Ref. 35].

Chevrons are geometrical corrugations on the cylindrical exhaust of either the primary jet (core) or secondary one (fan). Core chevrons directs flow inward with respect to the jet that reduce noise during take-off. Fan chevrons are generally parallel to the engine axis and reduce shock-cell noise [Ref. 32].

Noise from the airframe is due to landing gear and high lift devices (HLD). Geometry is the key factor to reduce landing gear observability. Testing using bogie fairing allowed an overall reduction of 2.0 EPNdB for the landing gear and 0.4 EPNdB for the aircraft as a whole. A second concept, known as "slow down flow", places cables, wires, and accessories in front of the main strut or behind the strut where the flow velocity goes to zero. This concept allows aircraft noise reduction, at landing, of about 2 EPNdB and a further 0.5 dB reduction can be gained from plain perforated or even porous fairings [Ref. 32]. High lift devices (HLD) uses porous materials on the edge surface, slat chevrons or even fractal spoilers for noise reduction. These methods have been studied in 2D within TIMPAN exhibiting a slat noise reduction of 2 EPNdB. The concept of porous materials is to avoid sudden flow discontinuities. Slat chevrons use corrugations on the trailing edge to suppress coherent vortex structures in the gap. Fractal spoilers limit or suppress the noise originating from both the spoilers side edges and the interaction of the turbulent

18

spoiler wake with the downstream flap. Another advanced idea is to utilize adaptive material for the leading edge that would suppress slat gaps [Ref. 32].

2.4 <u>Entropy</u>

Shigeo Hayashibara et al. used entropy to determine turbomachinery stage efficiency through two-dimensional cascade measurements [Ref. 36].   The authors understood that the compressor stage efficiency was difficult to obtain due to complexity of the flow field. They also opted out of conducting tests for turbomachinery under full-scale high temperature rotating flow conditions. Instead, the stage efficiency was determined, as a function of the entropy generation rate that was a function of wake velocity profile. The efficiency was determined by two relationships [Ref. 37]. One in terms of total temperature ratio and change in entropy per unit mass, and the other in terms of total pressure ratio and change in entropy per unit mass. The next step was to determine entropy generation rate. The authors looked into the University of Limerick (UL) gas turbine team that measured entropy generation rate using cascade wind tunnel [Ref. 38-40]. UL determined that entropy generation rate was the mass flow rate multiplied by change in entropy per unit mass across the lower to the upper edge of the wake.

Experimental and computational techniques investigated entropy generation in the wake and boundary layer. Experimental measurements in the wake of a compressor cascade model was used to validate computational calculations for the same cascade model. Computational calculations were repeated, but in air, while keeping Reynolds number constant. This was done due to lack of information about 'R' in water, which is needed for their entropy generation rate equation. Results obtained from experimental and computational cases were integrated along the blade surface to obtain total entropy generation rate per unit span. The authors used a NACA 65-(12)10 profile blade for their experimental and computational method and maintained a chord Reynolds number of 8500.

The experimental method used a closed return-type water table facility. The facility consists of a settling chamber, $3.5' \times 6'$ long test section, return tank, impeller pump, and sluice gate. The sluice gate is used to obtain supersonic flow by lowering the gate to increase stagnation water level in the settling chamber. Since flow speed desired was subcritical, they did not use the sluice gate to achieve their desired speed.

To visualize flow, the test section was seeded with hydrogen bubbles, by placing a cathode wire by the trailing edge and an anode wire downstream. A short electrical pulse is passed through the wire that produces a thin column of hydrogen bubble. Initially the bubbles are parallel to the wire but deform due to the local velocity profile. They maintained a constant electrical pulse rate to generate a successive curved bubble line, known as the "time-lines". A Charged Couple Device video camera and VCR system with a time code generator captured the hydrogen bubble time-line. These images were analyzed using MATLAB® to determine the conversion factor between pixels in the image and actual physical distance.

19

This was achieved by placing an image of known size with a gridline pattern of 1-inch wide squares in the test section of the water table. The hydrogen bubble time-line was determined, from the image, by knowing the time required to reach its position. This distance is converted into velocity by noting the frame number imprinted on the video by the time code generator.

For the computational method, FLUENT® (Computational Fluid Dynamics software) determine the wake flow. Structured-unstructured hybrid-mesh grid system for the boundary layer computation was utilized. The structured mesh was implemented near the blade surface while the rest of the domain had an unstructured triangular mesh. In order to validate the computational results with experimental results, the velocity data from the CFD model was extracted at the same location of the hydrogen bubble wire in the water table experiment.

The experimental and CFD results were compared. The water table cascade wake results were in good agreement with CFD wake flow simulation at a Reynolds number, based on chord, of 8500. The trend obtained were that the freestream flow increased as the stagger angle was increased. The same trend was observed when the solidity was increased from 1.5 to 2.0 and that the physical size of the wake decreased as the solidity increased. It was determined that the decreased wake size was a result that the channel width was narrowed as the solidity was increased.

The entropy generation rate per unit span '$\dot{S}''$' was determined at three locations (1.0, 1.5, and 2.0 inches) downstream for comparison purposes. The results exhibited that the extent of entropy generated increased as solidity and stagger angle increased for each location. The wake results were in good agreement with the results for the entropy generation rate based on a detailed boundary layer velocity profile. The authors concluded that they were successful in determining the entropy generation rate based on the wake velocity profile and the rate trend showed an increase in entropy as the stagger or solidity increased.

Michel Mansour et al. describe a recently developed miniature fast response entropy probe at ETH Zurich [Ref 41]. Their motivation was the need to determine loss generation mechanisms of turbomachines. The probe was originally designed by Ng and Epstein [Ref 42], it consists of a piezoresistive sensor and a pair of thin-film gauges that measure unsteady pressure and temperature, respectively. The detailed design, manufacturing, and calibration of the probe are found in reference 41 and 42. The authors used this probe in three applications; measurements in a centrifugal compressor, film cooling configurations, and an axial turbine. The sensors principle components are a fast response aerodynamic probe (FRAP) and an unsteady total temperature probe based on thin-film technology. The authors conclude that the sensor can operate at high Mach numbers and large temperature gradients which proves the sensors robustness and that the entropy probe can provide new information into energy loss in mechanisms.

3   <u>Theoretical Consideration</u>

Based on literature review this section discusses the sphere and wing signatures and the derivation of Gibbs equation.

3.1 <u>Sphere and Wing signature</u>

Findings on how to reduce IR, radar, and noise is theoretically applied to the sphere and the wing. For IR signature, since there is no propulsion system, it is primarily dependent on aerodynamic heating. Based on the general equation (2.1), the difference between airframe temperature and ambient temperature was 0.18% and 0.07% for the sphere and wing, respectively. Radar signature reduction is obtained, through shaping and radar-absorbing material. In addition, to get an estimation of the RCS of the sphere and wing, the general equations shown below are used. For the wing, a flat plate and wavelength of 1m is assumed to make calculations simpler.

$$\textbf{Sphere} \qquad \sigma_{max} = \pi r^2 \tag{3.1}$$

$$\textbf{Flat plate} \qquad \sigma_{max} = \frac{4\pi w^2 h^2}{\lambda^2} \tag{3.2}$$

From equations (3.1) and (3.2) the estimated RCS of the sphere and wing are -19.9dBm^2 and -10.6dBm^2, respectively. This is very small, 0.010 m^2 and 0.087 m^2 to be exact. For noise signature, the main cause is from the engine and is proportional to the incoming flow speed. Since there is no propulsion system and the flow velocities are Mach 0.1 and Mach 0.07, for the sphere and wing respectively, the noise generated is considered negligible.

3.2 <u>Gibbs Equation Derivation</u>

In the early 1850's a German physicist, Rudolf Clausius, discovered the concept of entropy. He discovered entropy from its origin in Carnot cycles. Clausius formulated the first-ever mathematical formulation of entropy. He stated that if two transformations, without necessitating any other permanent change can mutually replace one another be called equivalent, then the generations of the quantity of heat from work at a temperature has an equivalence-value. Now known as entropy, 'S' [Ref. 5].

Since entropy is difficult to measure experimentally, it can be determined through Gibbs equation. This equation requires the measurement of two state properties; total pressure and temperature. To determine Gibbs equation in terms of pressure and temperature, the use of the 1st and 2nd Law of Thermodynamics is required. Equation (3.3) shows that the change in entropy is due to the change in heat transfer of the system divided by temperature in reversible processes. Equation (3.4) represents the differential form of equation (3.3) which is considered an accurate definition [Ref. 6].

$$\Delta S = \frac{\Delta Q}{T} \tag{3.3}$$

$$dS = \frac{dQ}{T} \tag{3.4}$$

To evaluate the change in entropy, the 1st Law of Thermodynamics is considered, equation (3.5). It shows that internal energy is defined as change in heat transfer and change in work done by the system.

$$dE = dQ - dW \tag{3.5}$$

Substituting the definition of reversible work for a gas into equation (3.5) results in equation (3.6).

$$dQ = dE + Pd\mathcal{V} \tag{3.6}$$

Although the substation of reversible forms of heat and work into the 1st Law of Thermodynamics to obtain the Gibbs equation, it is valid for irreversible processes as well. The lost work due to friction is dissipated into heat as an irreversible component of heating. The definition of enthalpy is now introduced, equation (3.7). Enthalpy is substituted into equation (3.6) after it is re-written in its differential form, equation (3.8).

$$H = E + P\mathcal{V} \tag{3.7}$$

$$dH = dE + Pd\mathcal{V} + \mathcal{V}dP \tag{3.8}$$

Substituting equation (3.8) into (3.6), results into (3.9) where the two PdV terms cancel out. This simplifies the final equation into (3.10).

$$dQ = dH - \mathcal{V}dP - Pd\mathcal{V} + Pd\mathcal{V} \tag{3.9}$$

$$dQ = dH - \mathcal{V}dP \tag{3.10}$$

The next step is to analyze equation (3.10) for an ideal gas. Equation (3.11) is the ideal gas law and equation (3.12) is change in enthalpy for temperature difference of an ideal gas, also known as a constant pressure process.

$$P\mathcal{V} = RT \tag{3.11}$$

$$dH = c_p dT \tag{3.12}$$

Substituting the value of $\mathcal{V}$, from equation (3.11) and the definition of dH, equation (3.13) is obtained.

$$dQ = c_p dT - \frac{RT}{P} dP \tag{3.13}$$

Taking equation (3.13) and substituting it into the differential form of entropy, equation (3.4), leads to (3.14). Taking temperature to the other side of the equation lead to equation (3.15).

$$TdS = c_p dT - \frac{RT}{P} dP \tag{3.14}$$

$$dS = \frac{c_p}{T} dT - \frac{R}{P} dP \tag{3.15}$$

Integrating the differential form of entropy results in an equation where change in entropy can be related to pressure and temperature, shown in equation (3.16).

$$\Delta s = c_p \ln \frac{T_2}{T_1} - R \ln \frac{P_2}{P_1} \tag{3.16}$$

Equation (3.16) is altered so that change in entropy calculated will be between an arbitrary point '2' in the wake of the object and the reference pressure and temperature. It is noted that total pressure and total temperature at point '2' will be used. This leads to equation (3.17) which will used for computation fluid dynamic (CFD) and wind tunnel analysis.

$$\Delta s_{2-Ref} = c_p \ln \frac{T_{t2}}{T_{Ref}} - R \ln \frac{P_{t2}}{P_{Ref}} \tag{3.17}$$

Since the investigation of the sphere and wing is adiabatic. T_{t2}/T_{Ref} equals 1, therefore entropy is only based on change in pressure.

4   Computational Fluid Dynamic Analysis

Computational fluid dynamic analysis (CFD) performed on the sphere and wing involves determining the total pressure signature and entropy trail of the model at three non-dimensionalized distances away from the model. STAR-CCM+ [Ref. 44] was used to run CFD simulations. The reference values, based on wind tunnel test section, for the simulations for the sphere and wing is as follows:

- P_{Sphere} = 99300 Pa
- P_{Wing} = 99180 Pa
- T = 298 K
- V_{Sphere} = 35.76 m/s (80 mph)
- V_{Wing} = 22.35 m/s (50 mph)
- ρ = 1.159 kg/m^3

The difference in reference pressure, for the sphere and wing, was due to wind tunnel measurements were conducted at difference times. The wing has a slower flow speed because during wind tunnel operations the wing exhibited intense fluctuations. Therefore, the flow speed was reduced from 80mph to 50mph. The simulations were ran at a Reynolds number, based on diameter and chord, of 257000 and 201000 for the sphere and wing. The simulation signatures were evaluated at 1.05D, 6D, and 23D, from the aft edge of the model, where 'D' is the chord of the wing or diameter of the sphere. The wing was simulated from 0 to 16 degrees, angle of attack, at increments of 2 degrees. This chapter also discusses how the simulation and parameters are set up and determined. The results of the CFD analysis are in the Results chapter.

4.1 Models

The sphere and wing can be observed in Figure 4.1 and Figure 4.2

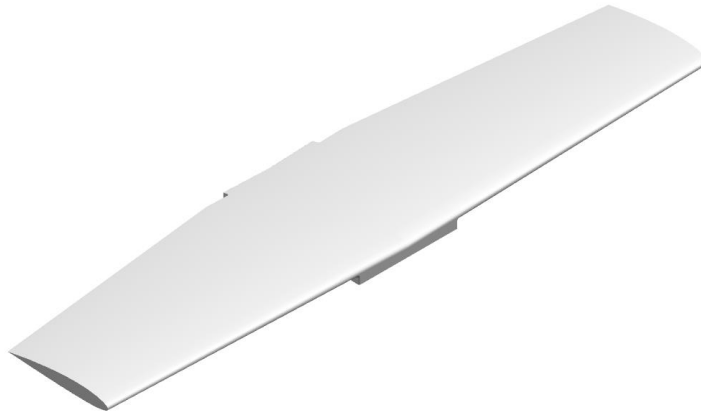**Figure 4.1: CAD - Sphere Model**

Figure 4.2: CAD - Wing Model

The main dimensions of the sphere and wing are in Table 4.1 and detailed dimensions are in the Appendix.

Table 4.1: Sphere and Wing Specifications

	c_{tip} (in)	c_{root} (in)	b (in)	A (in^2)	Γ (deg)	$\Lambda_{L.E.}$ (deg)
Wing	4	5.36	24	115.6	2	0
	ø (in)	A (in^2)				
Sphere	4.5	15.9				

4.2 STAR-CCM+

STAR-CCM+ is a multidisciplinary simulation software developed by CD-Adapco [Ref. 44]. This program is used to mesh and simulate the two desired models. The remainder of this chapter will discuss the determination of the domain size, mesh, and physics model.

4.2.1 Domain Geometry

The dimensions for the sphere domain and wing domain are $45 \times 135 \times 22.5$ and $20 \times 171 \times 40$ inches, respectively. The size of the domain must be large enough to allow incoming flow to fully develop

before it reaches the model and so that the domain walls does not interact with flow around the model. To save computational time only half the sphere and wing were simulated, since the models are symmetric. This was achieved by using a "symmetry plane". The symmetry plane boundary is identical to the solution that would be obtained by mirroring the mesh about the symmetry plane [Ref 45] which is exhibited in Figure 4.3 and Figure 4.4. The figures show the domain of the sphere and wing, with the assigned boundary conditions inlet, outlet, wall, and symmetry plane. The location of the sphere center is 22.50 inches away from the inlet and walls. The location of the wing (leading edge) is 40 inches from the inlet, 10.15 inches from the top wall, and 9.85 inches from the bottom wall.
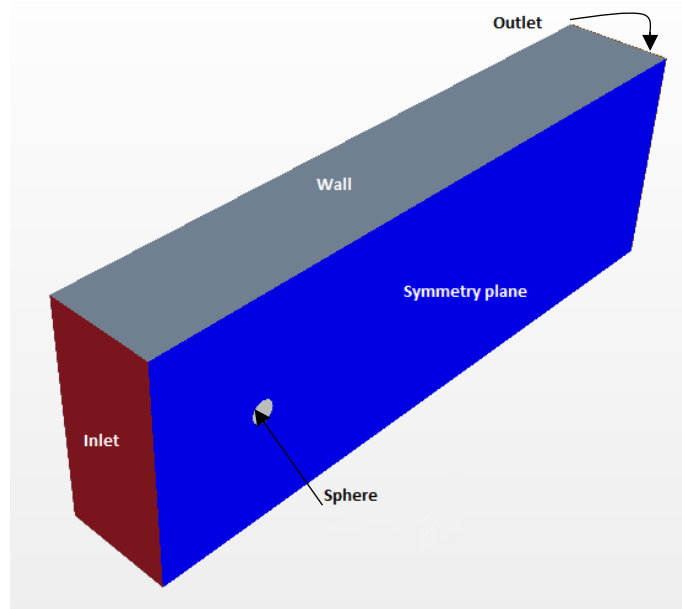
Figure 4.3: Sphere Domain
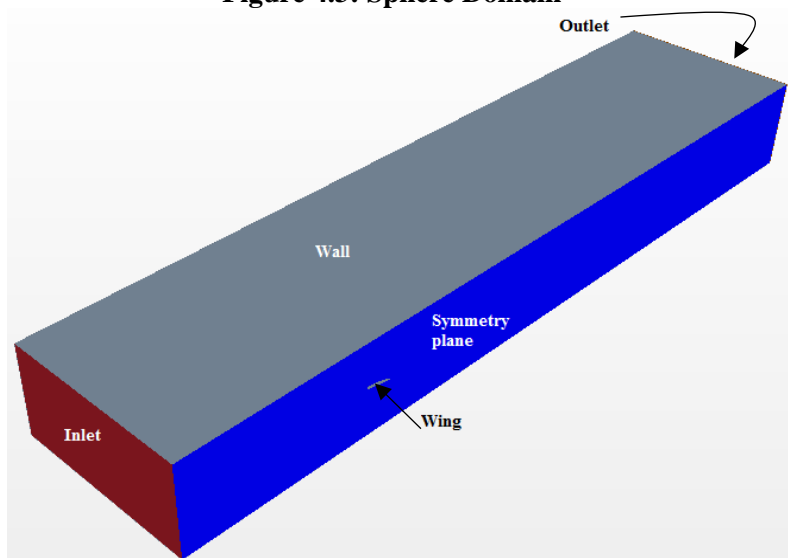
Figure 4.4: Wing Domain

4.2.2 Mesh

Automated parts based was used to mesh the model and domain. Surface cell size and cell growth rate can be adjusted so that the area of interest can be fine (more cells) and the remainder of the domain can be coarse (less cells). A polyhedral mesh was used for both models, as they are easy and efficient to build, requiring no more surface preparation than the equivalent tetrahedral mesh. Polyhedral meshing also contains five times fewer cells than the tetrahedral mesh [Ref. 45], saving on computational time. Since this study is interested in the wake of the model, a wake refinement was added to the model, illustrated in Figure 4.5 and Figure 4.6 as well as the mesh for the wing and sphere.
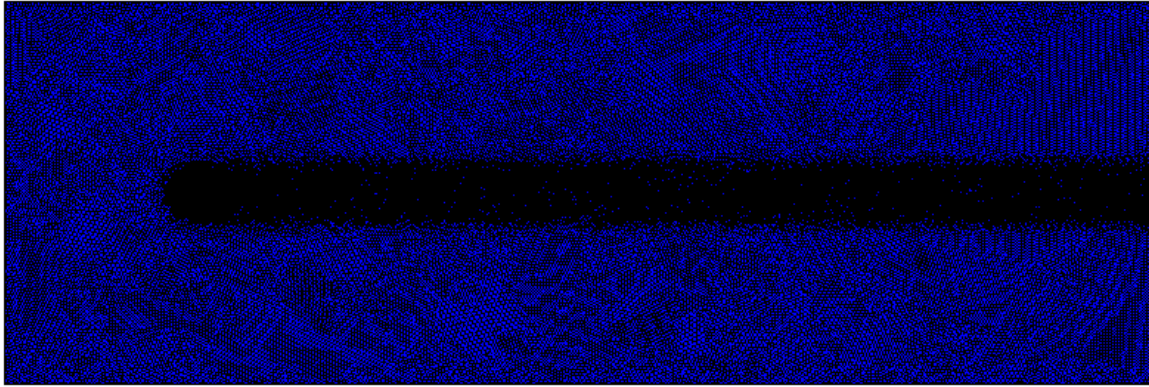
Figure 4.5: Sphere Mesh
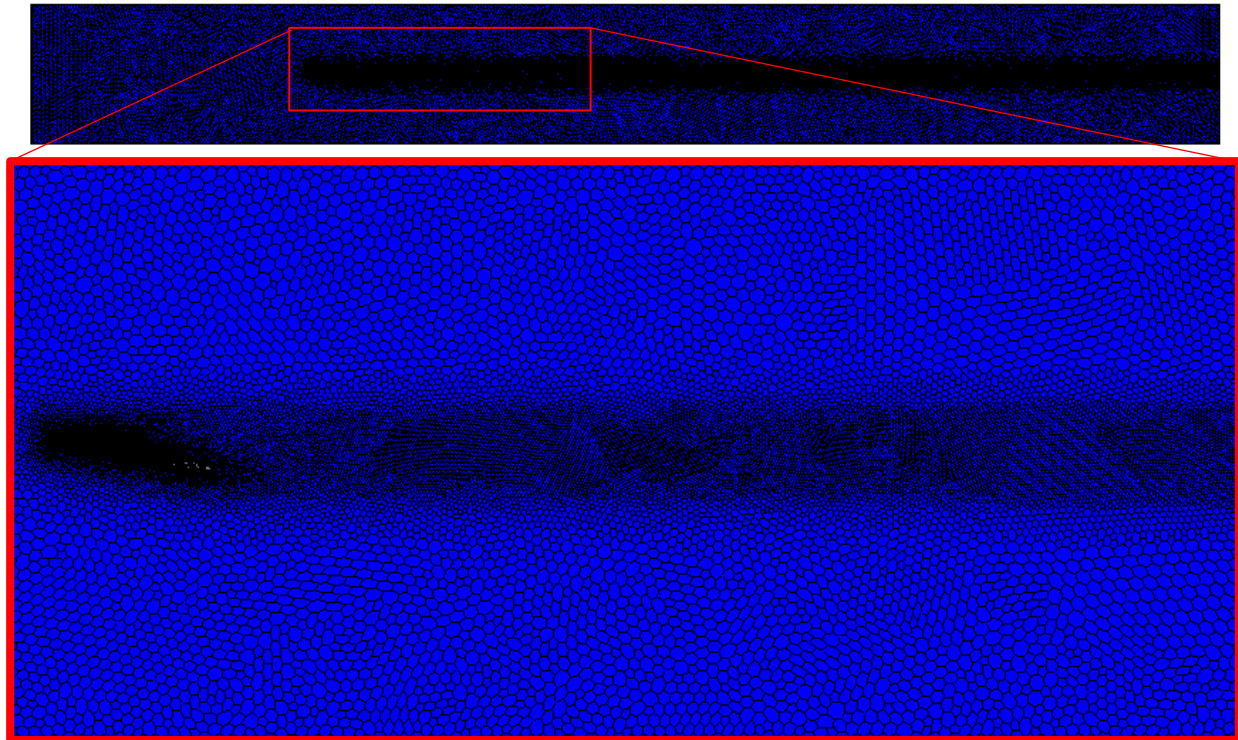
Figure 4.6: Wing Mesh [zoomed at the Wing]

Figure 4.5 and Figure 4.6 show that the finer mesh is located within the area of the model and for the wake refinement whereas the rest of the domain is coarse. Prism layer cells are added to the sphere and wing, to accurately model the boundary layer as observed in Figure 4.7 and Figure 4.8.
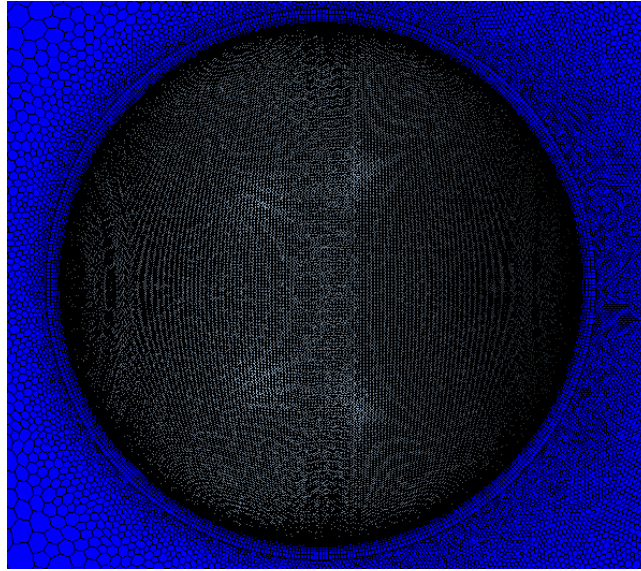
Figure 4.7: Sphere Prism Layers
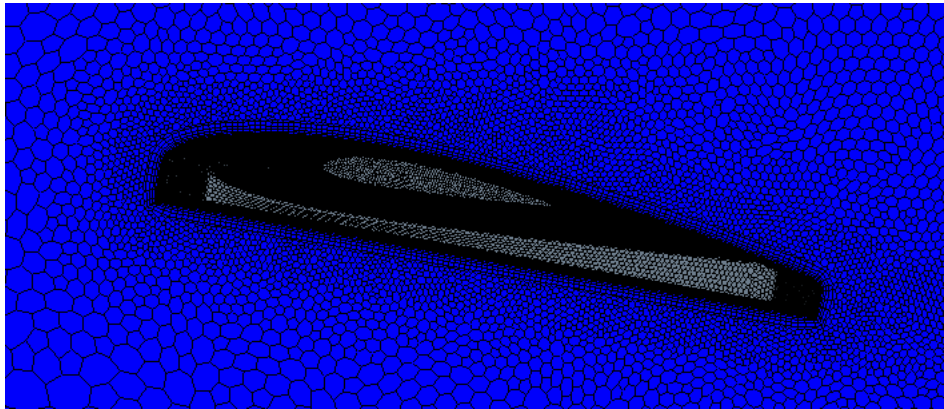
Figure 4.8: Wing Prism Layers

It is important to iterate the overall domain mesh size from, coarse to fine, to determine the optimal mesh. This is obtained by starting with an initial mesh (cell count), running the simulation until it converges (usually once the residuals are below 10^{-4}). After the first simulation, several iterations with finer meshes proceed until the desired result of the refined mesh were within or less than 5% of the previous simulated mesh. For the sphere and wing, it was found that the optimal cell count was 5.5E6 and 6.9E6, respectively. Figure 4.9 displays the trend of coefficient of drag, as the mesh domain is refined. It is observed that the mesh study for the wing was conducted for 0 and 2 degrees angle of attack. This was to solidify the optimal mesh domain.
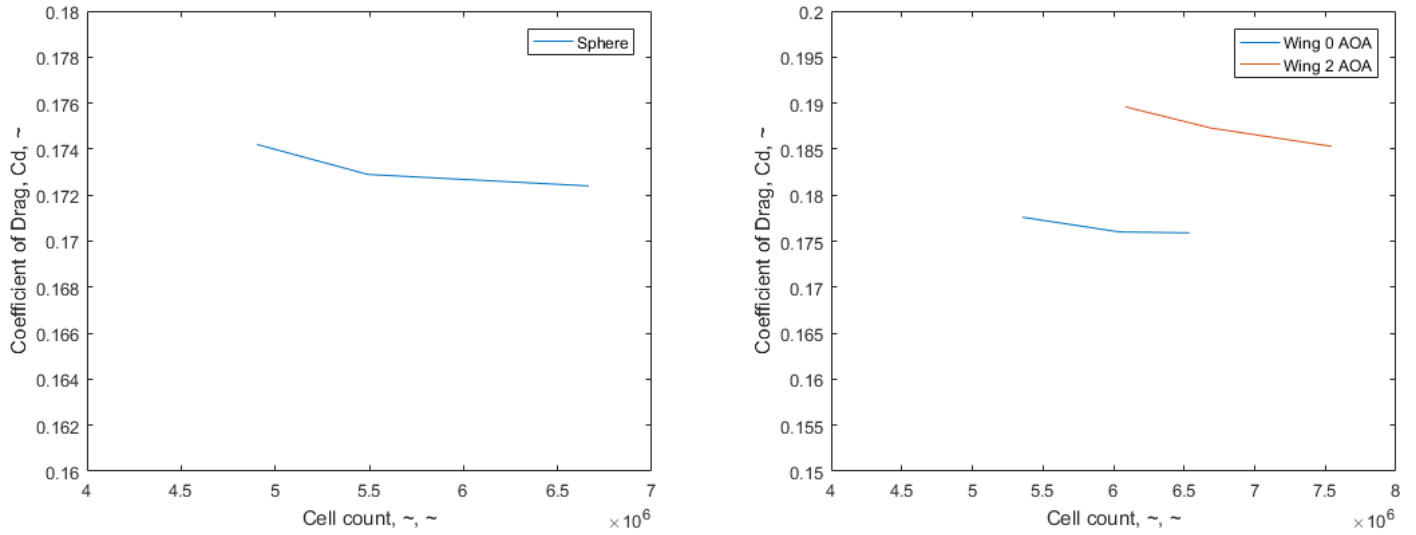
Figure 4.9: Cd v Cell Count

Table 4.2 shows the results of the cell count study and the percentage difference between mesh refinements. The percentage difference between models is sufficient to consider the optimal mesh is achieved, as the percentage difference is less than 5%.

Table 4.2: Sphere and Wing Mesh Refinement Analysis

Sphere					
Iteration	**Elements**	**Cd**	**Cl**	**Cd % diff**	**Cl % diff**
	(~)	(~)	(~)	(~)	(~)
1	4,904,158	0.1742	0.0092	~	~
2	5,491,539	0.1729	0.0074	0.752	23.4
3	6,665,538	0.1724	0.0072	0.290	3.33

Wing					
0 deg					
1	5,354,351	0.1776	1.3308	~	~
2	6,043,135	0.1760	1.3297	0.949	0.08
3	6,537,818	0.1759	1.3299	0.045	0.02
2 deg					
1	6,083,254	0.1896	2.4757	~	~
2	6,687,184	0.1873	2.4707	1.244	0.20
3	7,544,251	0.1853	2.4676	1.052	0.13

28

4.2.3   Physics Model

The physics model used for the sphere and wing is as follows:

- Steady
- Three dimensional (3-D)
- Ideal gas
- Turbulent
- Low y+ wall treatment

Steady state was selected because it was sufficient for the simulation to converge. Unsteady state could have been selected but it typically takes an order of magnitude more computational time to complete. 3-D and ideal gas were selected due to the nature of the investigation. The turbulence model was selected based on a journal article that studied turbulence modeling applied to flow over a sphere [Ref. 46]. The authors compare six turbulence models to their experimental data. Four Reynolds-averaged Navier-Stokes (RANS) models; which is the two-layer k-ε model of Chen and Patel [Ref. 47], k-ω model of Wilcox [Ref. 48], $\overline{v^2}$-f model of Durbin [Ref. 49], and S-A model [Ref. 50]. The last two models were LES dynamic eddy viscosity model [Ref. 51] and DES, which is a modification to the S-A model such that closure reduces to RANS in the boundary layer and to LES away from the wall [Ref 52]. Each turbulence model compared well with the experimental data. The best model was the k-ω model, which was used in the simulation of the sphere and wing. The k-ω model is a two-equation model that solves transport equations for turbulent kinetic energy and specific dissipation rate to determine the turbulent viscosity [Ref 45]. Low y+ wall treatment was selected to accurately capture the boundary layer.

5   Wind Tunnel Analysis

The purpose of wind tunnel analysis is to replicate and validate entropy signatures generated from CFD simulations. This was conducted using a wake rake that measured total pressure at various distances in the wake of the model. Then total pressure is inserted into equation (3.17) to determine entropy, to validate CFD results. The results of the wind tunnel analysis are in the Results chapter.

5.1   Wind Tunnel

The wind tunnel used is a closed circuit subsonic tunnel, located at the University of Kansas, Learned Hall. It has a $36'' \times 51''$ test section and a maximum speed of 200 mph. The tunnel is equipped with a six-component pyramidal strain-gauge balance and a computerized data acquisition system. It has a contraction ratio of 9:1 and a turbulence factor of 1.1 at 140 mph. The tunnel is powered by a 300 HP electric motor, equipped with a 4-blade variable pitch propeller [Ref. 53 and 54]. Figure 5.1 displays the layout of the wind tunnel. The schematic drawing of the tunnel is shown in Figure 5.2.

Figure 5.1: Subsonic Wind Tunnel
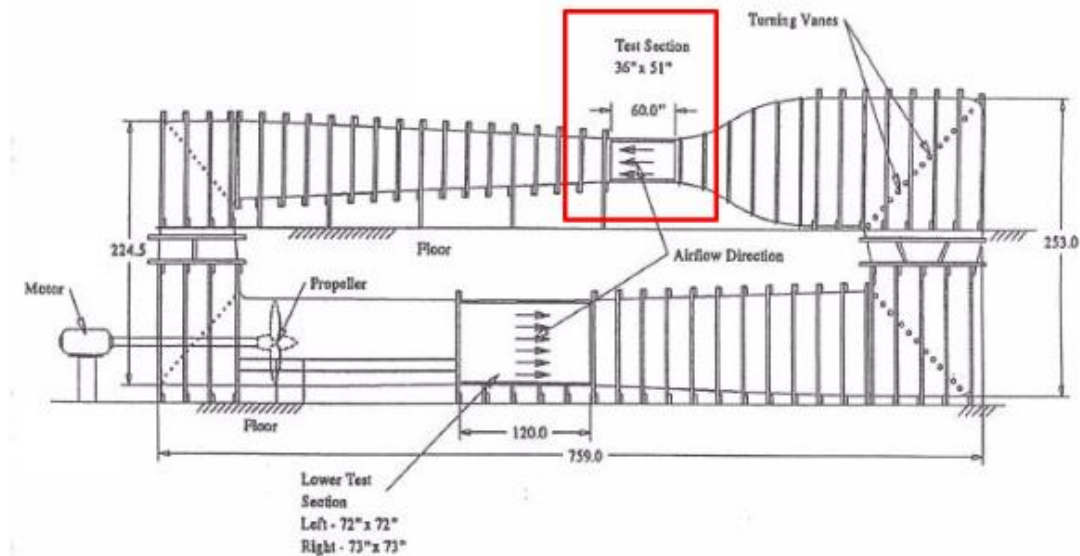
Figure 5.2: Subsonic Wind Tunnel Schematic Drawing [Not to scale - units in feet]

5.2 Test Stand

Since the wind tunnel test section is not equipped to have a wake rake mounted, a test board was fabricated, Figure 5.3. The incoming flow is from the bottom right of the figure. The blue dash line in the figure is where the attachment points are located. Detailed dimensions for each component is in the Appendix.
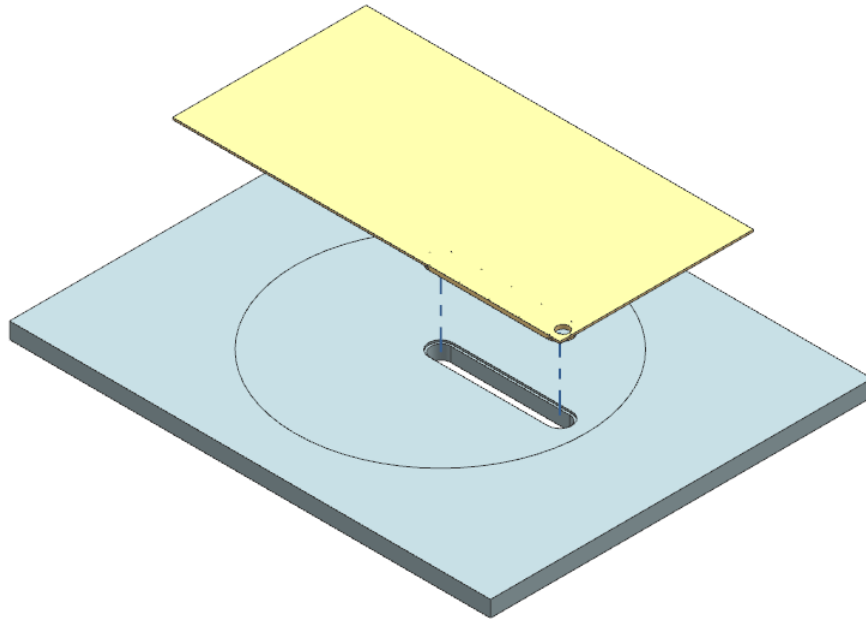
Figure 5.3: CAD - Wind Tunnel Test Section with Test Board

The slider apparatus was screwed to the board, allowing the wake rake to move freely in one direction, Figure 5.4. Once the slider was attached, the wake rake is fixed to the slider, Figure 5.5.
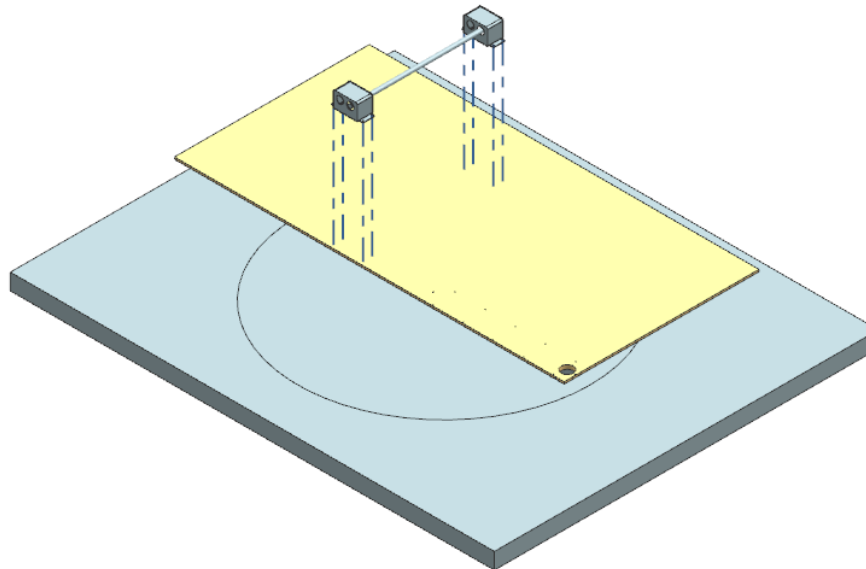
Figure 5.4: CAD - Slider Attachment to the Board
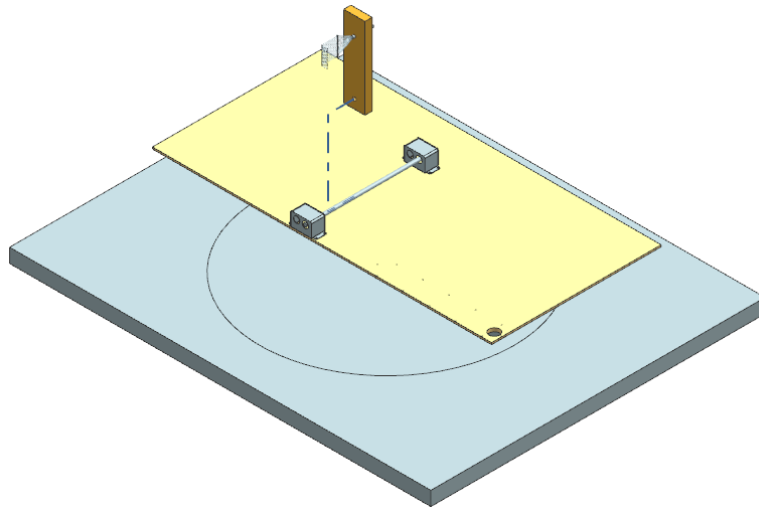
Figure 5.5: CAD - Wake Rake Attachment to the Slider

When mounting the wake rake, as observed in Figure 5.5, it is important to make sure the pitot tubes are aligned with the incoming flow. For a flat nose pitot tube, error in total pressure readings begins near a 10 deg flow inclination [Ref. 55]. The use of a laser lever made sure the pitot tubes were aligned and level to the incoming flow. Figure 5.6 shows the comparison of the CAD model of the test board with the sphere model and the finished product in the test section of the wind tunnel.
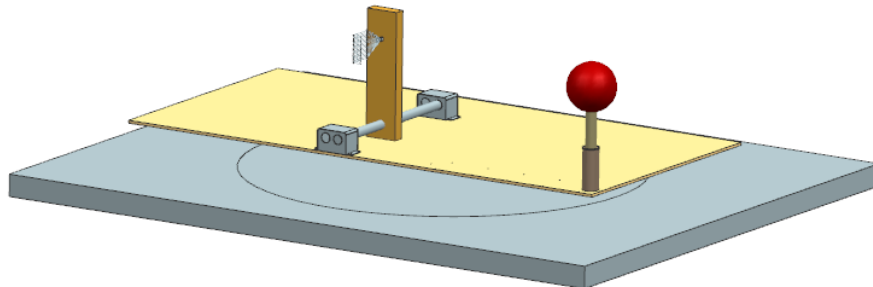
Figure 5.6: CAD v Test Board with Sphere Model Attached

The wing used the same test board as the sphere. An attachment part was fabricated for the wing so that it could be mounted to the test board, Figure 5.7.
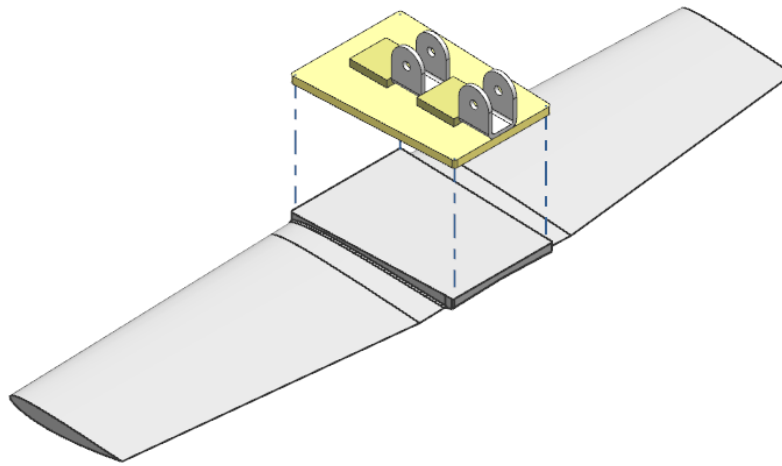
Figure 5.7: CAD - Wing Attachment

The wing mount had two attachment points, one in the center and one by the trailing edge of the wing. The center attachment is the pivot point allowing the wing to rotate about the span. The second attachment point varies angle of attack of the wing, using a lever, exhibited in Figure 5.8.
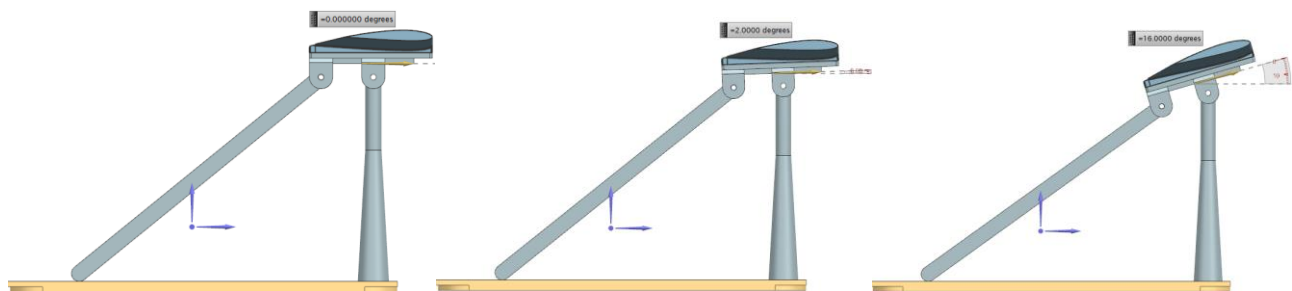
Figure 5.8: Varying Angle of Attack

Figure 5.8 demonstrates, as the angle of attack lever moves left, the angle of attack of the wing increases from 0 (left) to 2 degrees (center) and then 16 degrees (right). Figure 5.9 shows the comparison of the CAD wing model attached to the test board with the finished product in the wind tunnel test section.
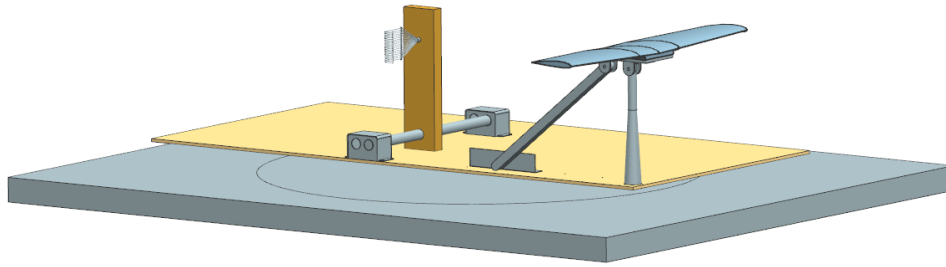
Figure 5.9: CAD vs Test Board with Wing Model Attached

5.3 <u>Pressure Sensor and Calibration</u>

The pressure sensor used is a MPXV7002DP, a piezoresistive transducers, that measures differential pressure based on dual ports. The differential pressure is between wind tunnel reference pressure and test section total pressures. The wake rake was connected to 7 pressure transducers, Figure 5.10.
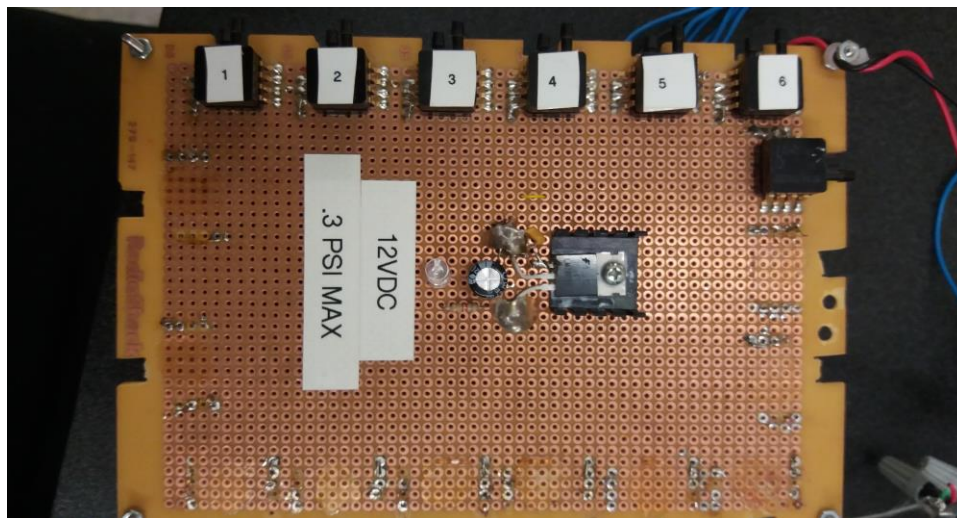
Figure 5.10: Pressure Sensor Board

The specification for the pressure sensor is a range of ± 2kPa and an accuracy of ± 2.5 % V_{FSS}. Where V_{FSS} is the difference between output voltage at maximum pressure and output voltage at minimum pressure [Ref. 56]. The sensor outputs a voltage reading based on differential pressure. To be able to read voltage output, sensors are connected to LabView, which allow voltage readings to be recorded for post-processing. Figure 5.11 displays the sensors wiring to LabView.
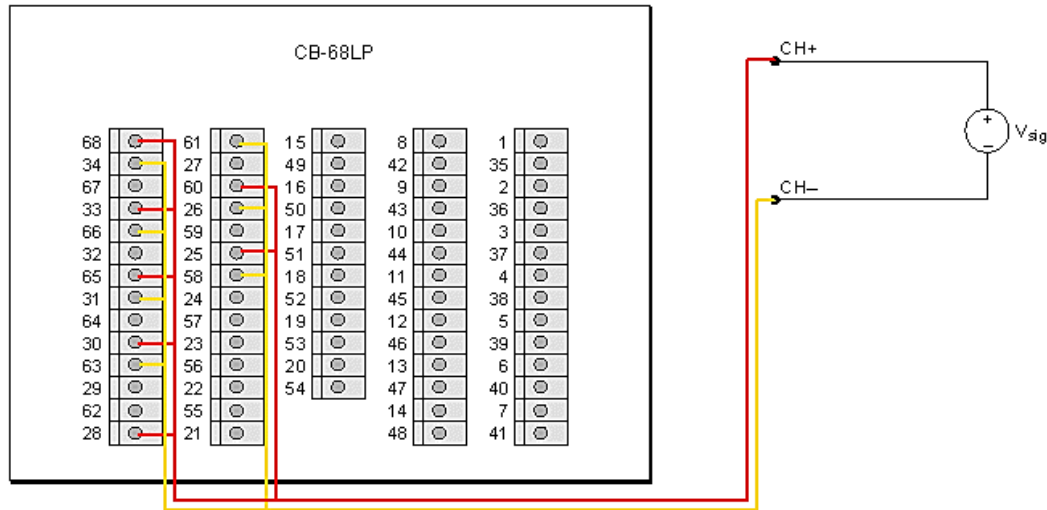
Figure 5.11: Sensor Wiring to LabView

The red line is power supply and the yellow line is ground. Probe 1 is wired into slots 68 and 34, probe 2 into slots 33 and 66, probe 3 into slots 65 and 31, probe 4 into slots 28 and 61, probe 5 into slots 60 and 26, probe 6 into slots 25 and 58, and probe 7 into slots 25 and 58. The sensors give an output voltage, to some corresponding differential pressure, which is not known. Therefore, the sensors need to be calibrated. Calibration was based on velocity and static pressure of the wind tunnel test section. Since these two parameters were known, the dynamic pressure was calculated and given the static pressure, total pressure was determined which corresponds to the output voltage from the sensors. The range of velocities used for calibration was from 0 to 85 mph in increments of 5 mph. The sample rate for the sensors was 1000 HZ. The wind tunnel test section temperature and pressure were 298 K and 99180 Pa, respectively, and the density was 1.159 kg/m^3. The calibration curves for each sensor (probe) are displayed in Figure 5.12.
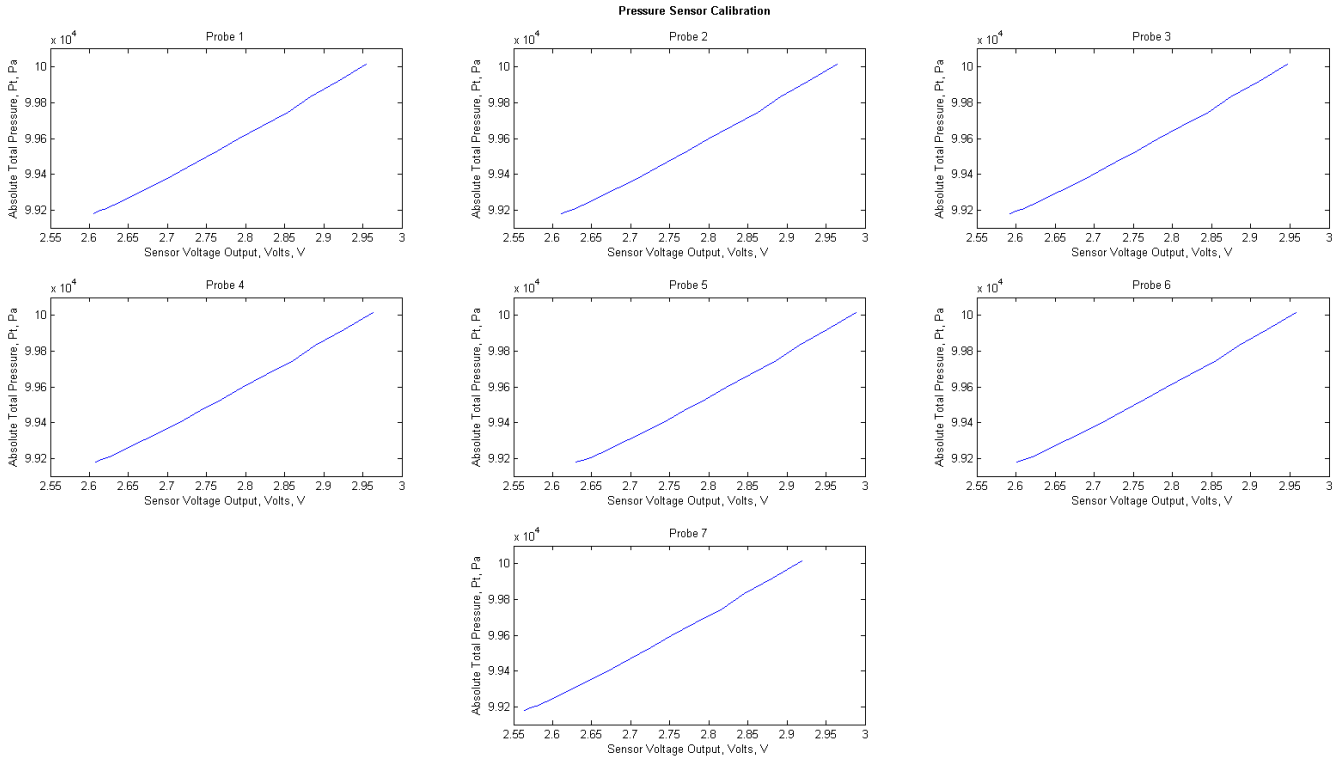
Figure 5.12: Pressure Sensor Calibration

The calibration curve for each pitot tube will be used to generate a quadratic equation which will be used to convert the sensor voltage output to its corresponding total pressure. These equations can be seen below, equation (5.1) to (5.7).

$$\text{Probe 1} \qquad y = 986.4x^2 - 3062.6x + 100458 \qquad \textbf{(5.1)}$$

$$\text{Probe 2} \qquad y = 1030.6x^2 - 3340.0x + 100866 \qquad \textbf{(5.2)}$$

$$\text{Probe 3} \qquad y = 1002.6x^2 - 3163.8x + 100636 \qquad \textbf{(5.3)}$$

$$\text{Probe 4} \qquad y = 973.5x^2 - 3035.0x + 100468 \qquad \textbf{(5.4)}$$

$$\text{Probe 5} \qquad y = 1048.8x^2 - 3511.1x + 101148 \qquad \textbf{(5.5)}$$

$$\text{Probe 6} \qquad y = 1018.8x^2 - 3279.6x + 100809 \qquad \textbf{(5.6)}$$

$$\text{Probe 7} \qquad y = 984.3x^2 - 3005.7x + 100409 \qquad \textbf{(5.7)}$$

Where 'x' is the sensor voltage and 'y' is the output total pressure.

6   Results

This section presents the results obtained by CFD and wind tunnel testing. Wind tunnel testing was conducted at arbitrary locations downstream, of the sphere and wing at 0 and 16 degrees, to validate CFD results.

6.1 Total Pressure signature CFD

CFD Total pressure for the sphere and wing are recorded in Figure 6.1 to Figure 6.10. The data displays the signatures at 1.05D, 6D, and 23D (starting from the top of each figure respectively) distance away from the model. Where 'D' is the diameter of the sphere and chord of the wing.

6.1.1   Sphere Total Pressure and Total Temperature signature CFD

Figure 6.1 exhibits the greatest total pressure distribution closest to the model, then dissipated downstream of the wake. It is also observed that the distribution matches the shape of the sphere, where the pressure values change around 200 Pa, which is very small.
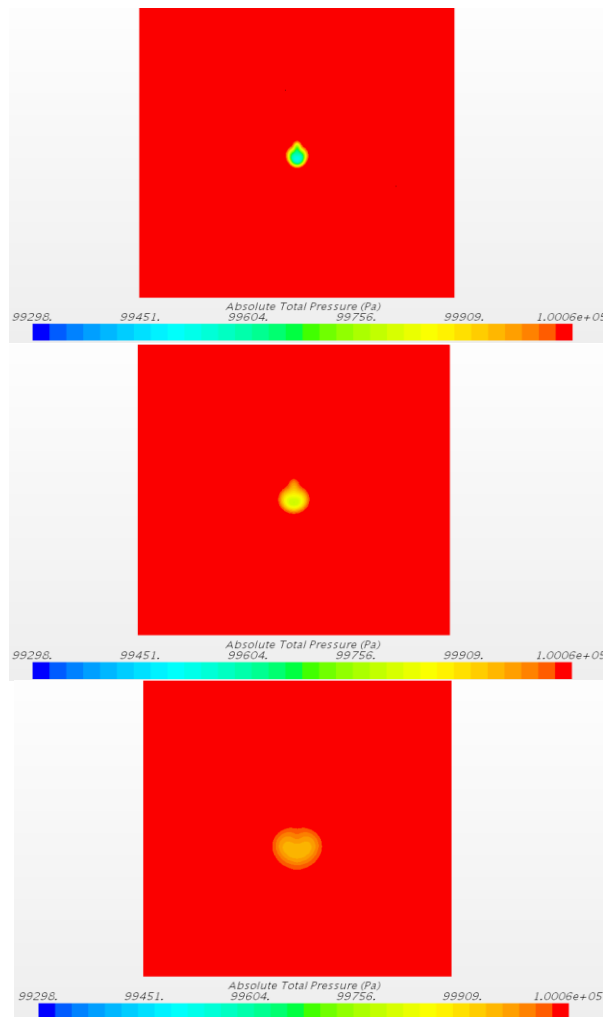
Figure 6.1: Sphere Total Pressure Signature

6.1.2 Wing Total Pressure signature CFD

Figure 6.2 to Figure 6.10 display the total pressure signatures from 0 to 16 degrees at 2 degree increments. The strongest signatures, top of each figure, were recorded closest to the model and then dissipates downstream. It is also observed that pressure signatures, from Figure 6.2 to Figure 6.8, are similar at each respective distance away from the model. They maintain the same signature until the flow separates. Flow separation is exhibited at 14 degrees and beyond, Figure 6.9 and Figure 6.10.
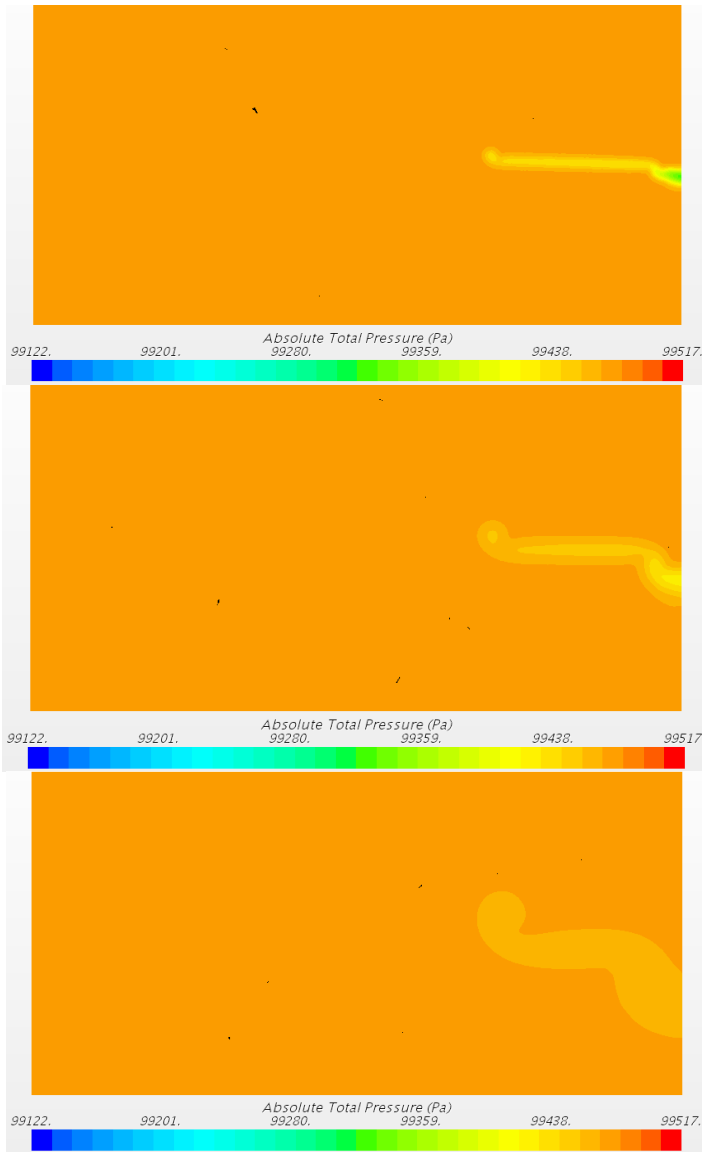
Figure 6.2: Wing Total Pressure Signature [0 deg]
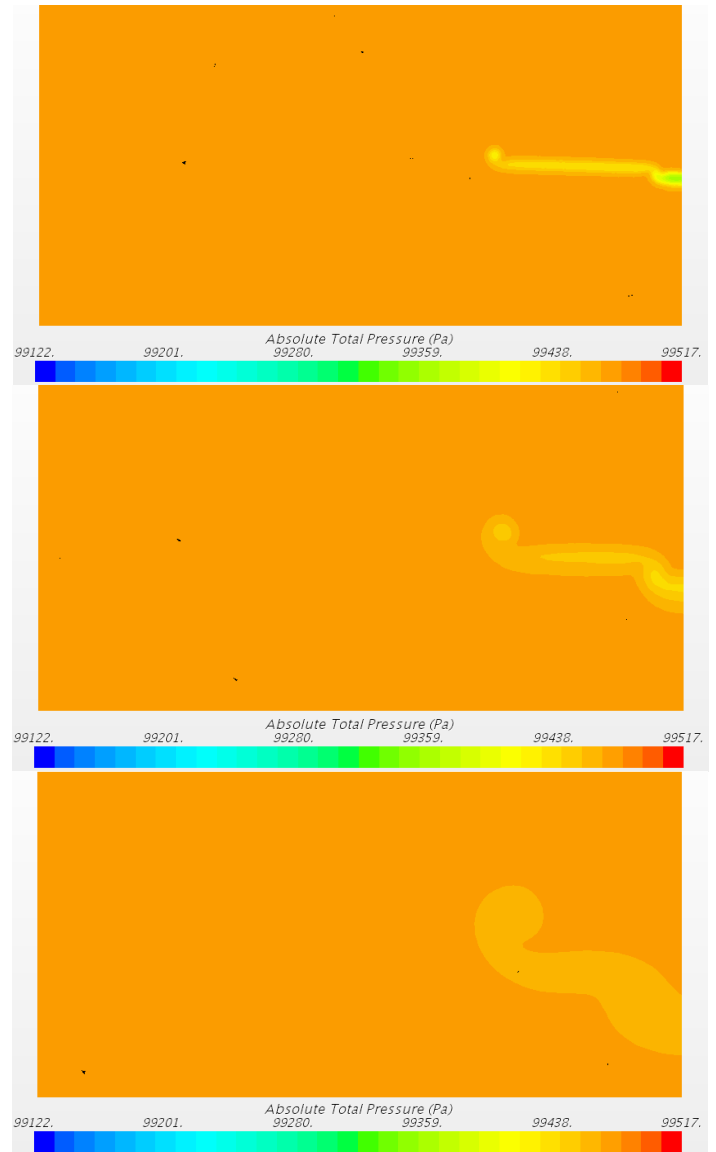
Figure 6.3: Wing Total Pressure Signature [2 deg]
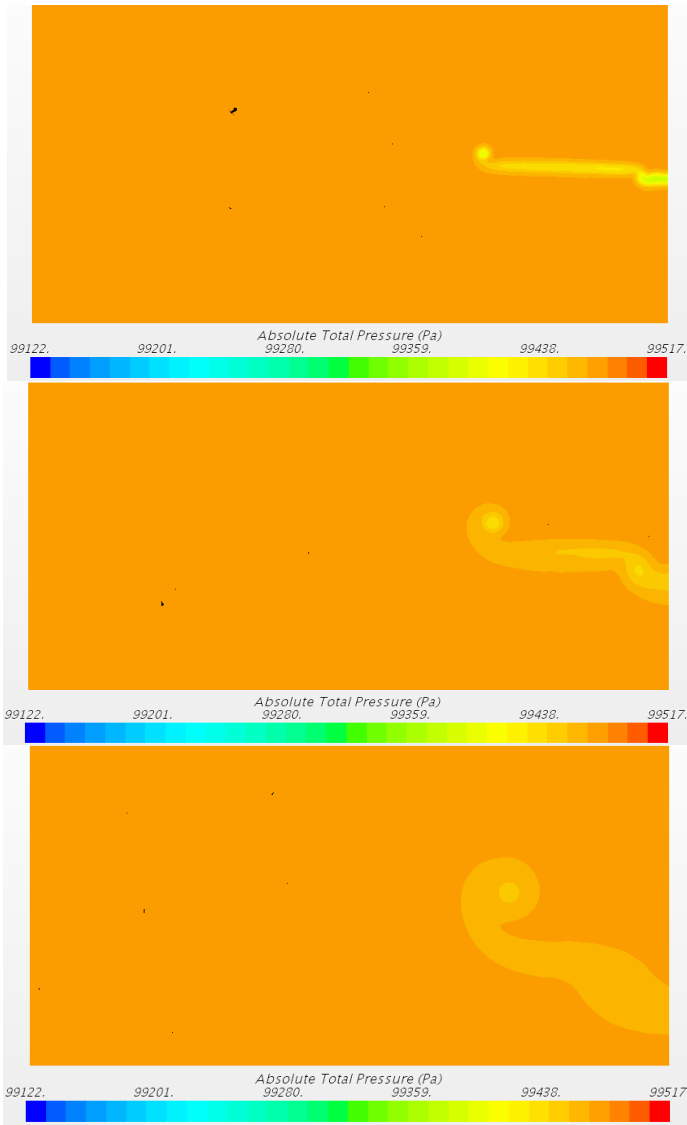
Figure 6.4: Wing Total Pressure Signature [4 deg]
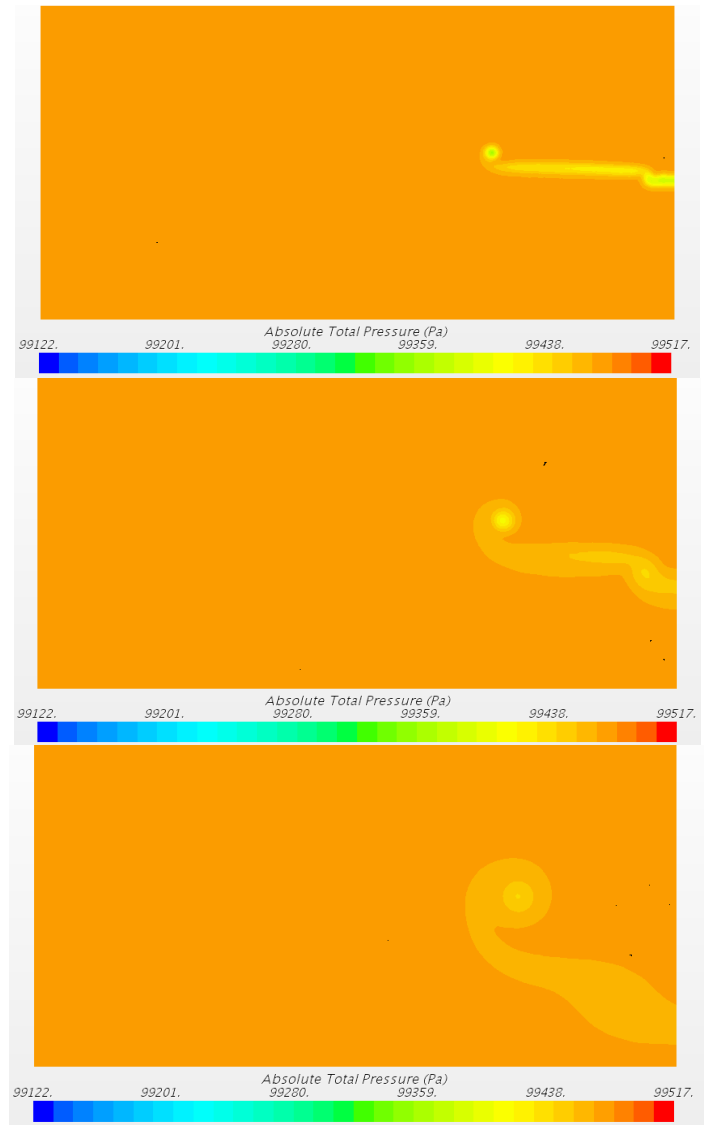
Figure 6.5: Wing Total Pressure Signature [6 deg]
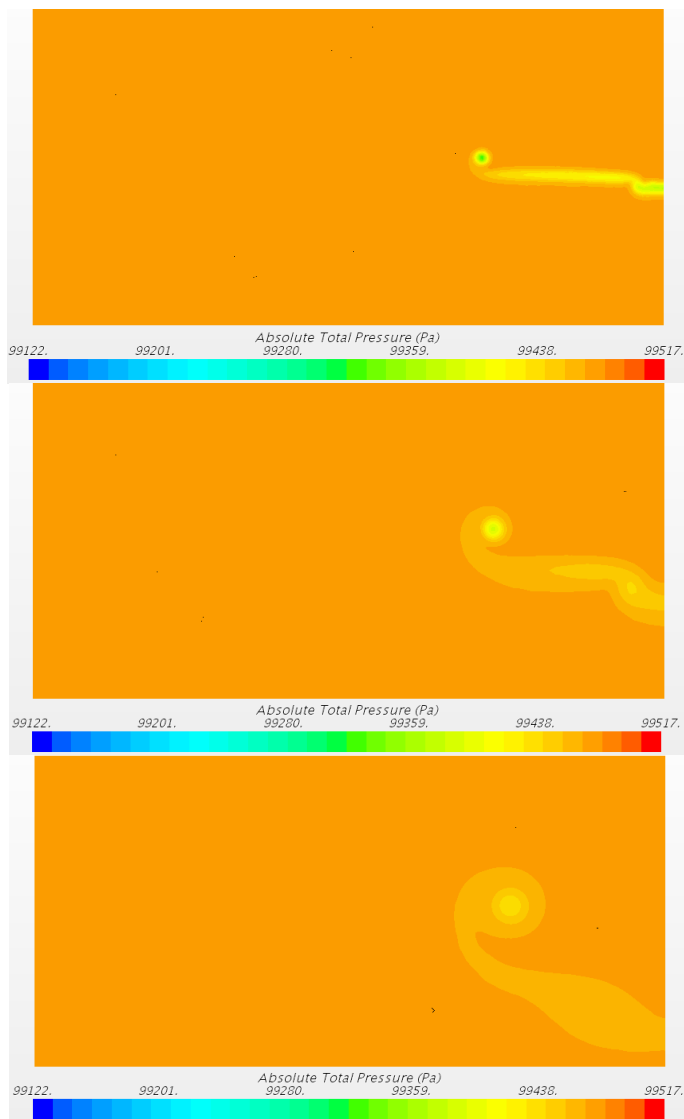
Figure 6.6: Wing Total Pressure Signature [8 deg]
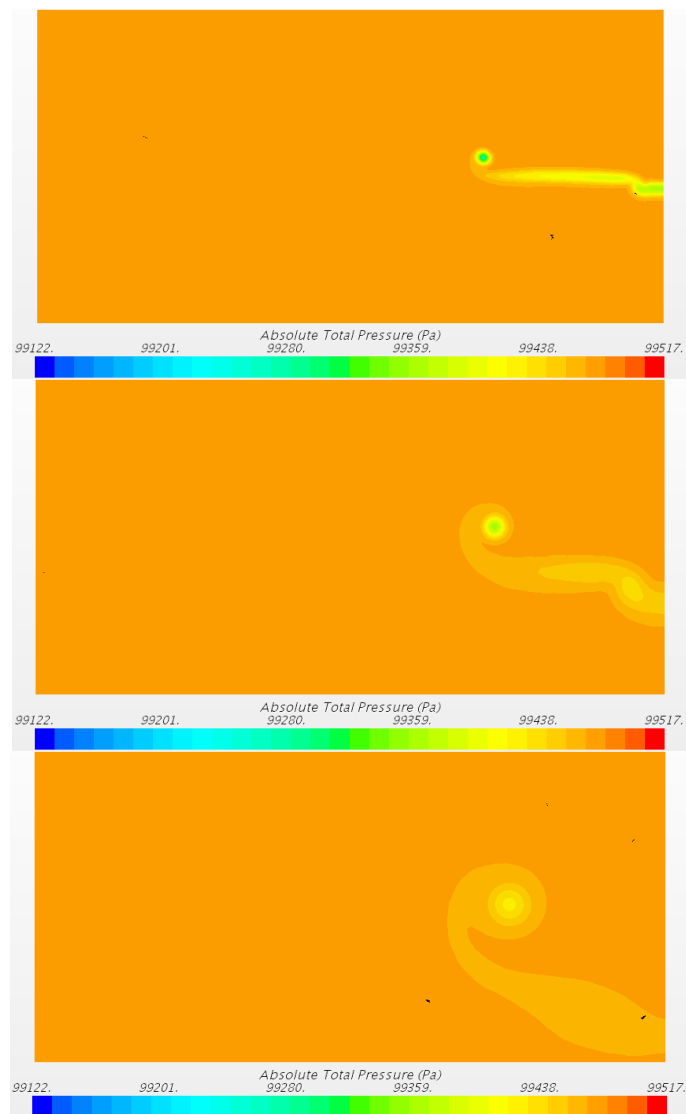
Figure 6.7: Wing Total Pressure Signature [10 deg]
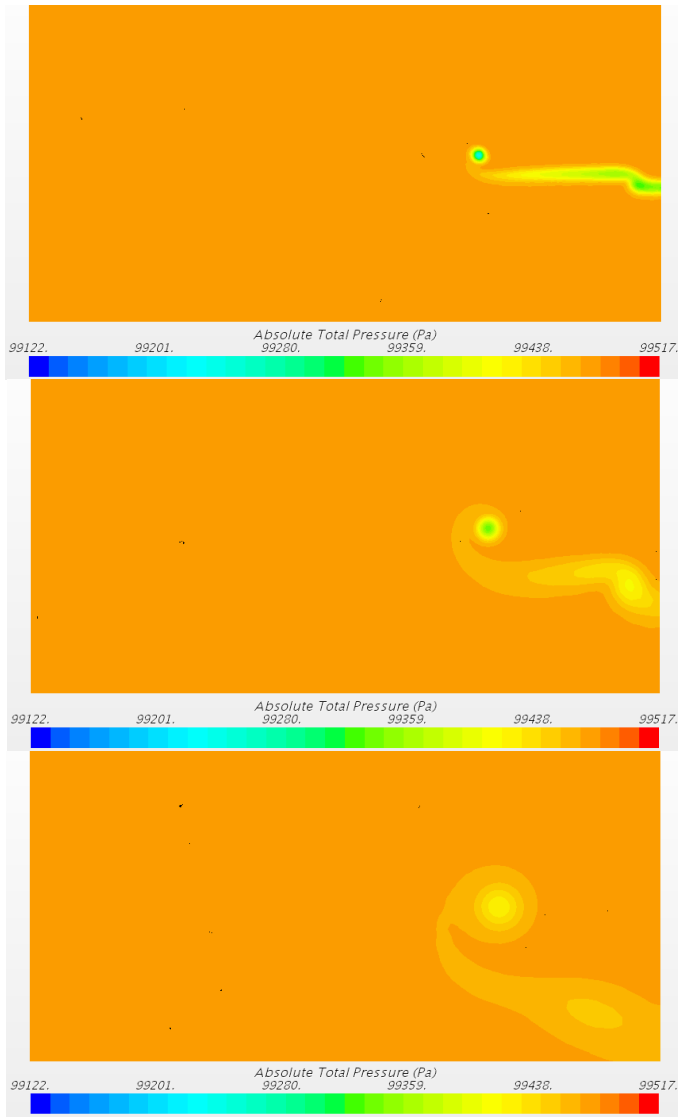
Figure 6.8: Wing Total Pressure Signature [12 deg]
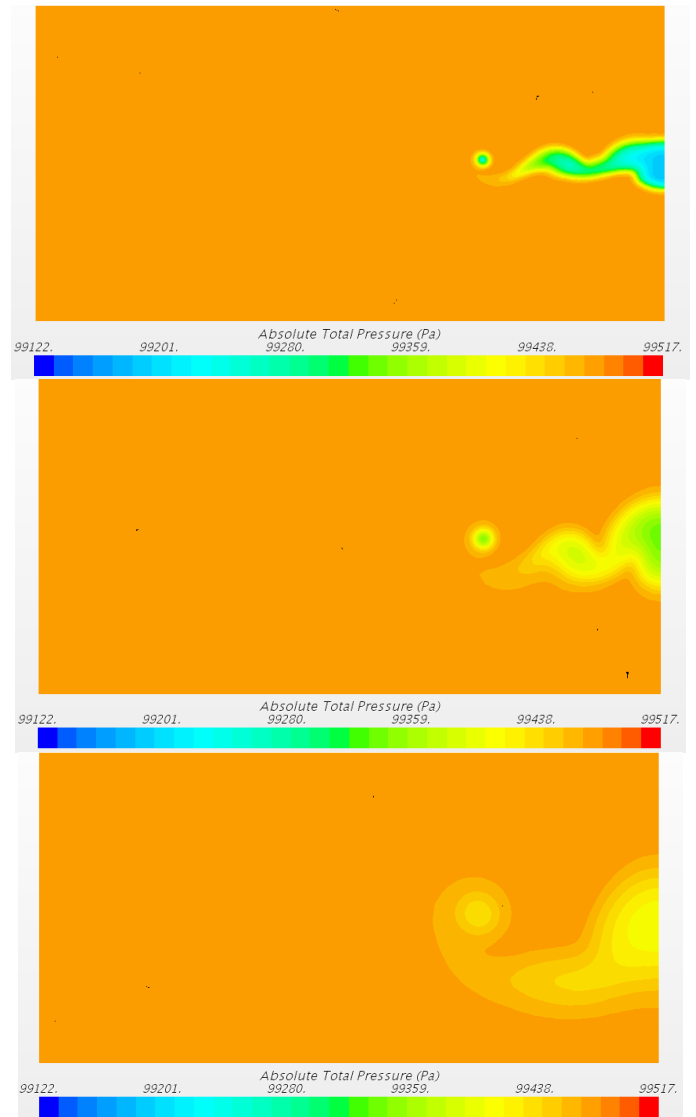
Figure 6.9: Wing Total Pressure Signature [14 deg]
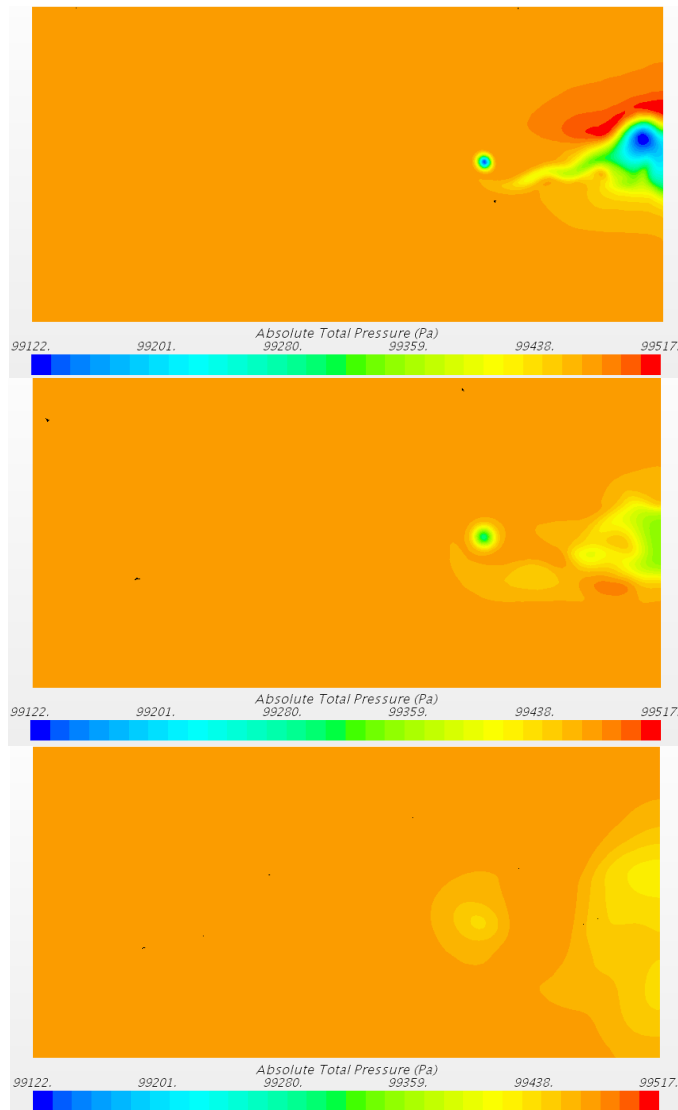
Figure 6.10: Wing Total Pressure Signature [16 deg]

6.2 Total Pressure from the Wind Tunnel

Total pressure wind tunnel measurement was used to validate CFD results. The sphere and wing were validated at arbitrary locations span-wise of the model. Validation could only be conducted at '1.05D' and '6D' distance away from the trailing edge of the sphere and wing due to size restrictions of the wind tunnel test section. Figure 6.11 shows the location of the probes, where the flow is going in the '-X' direction.
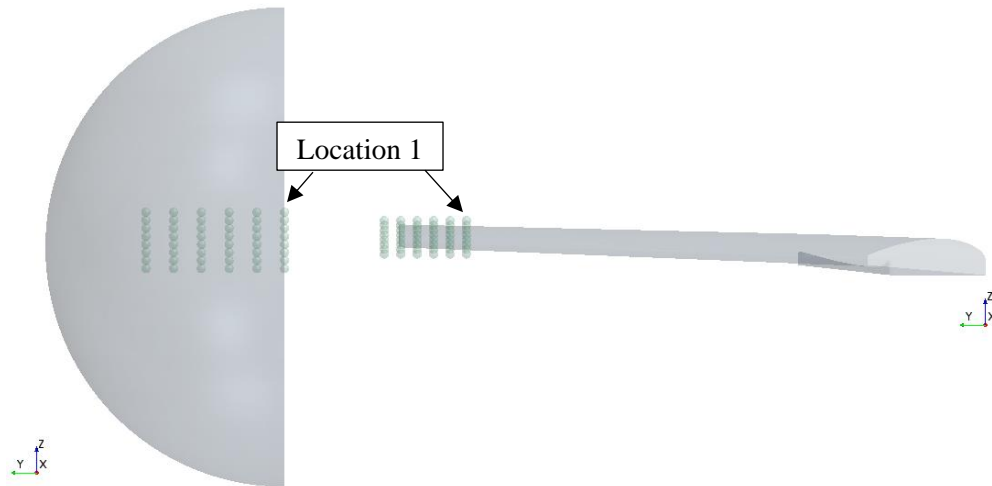
Figure 6.11: Sphere and Wing Probe Locations

Each "line" in the 'Z' direction, observed in Figure 6.11, represents the location of the wake rake. The spacing, in the 'Y' direction, between each location is 0.5 inches. The spacing between each probe, in the 'Z' direction, is 0.145 inches. The location of the probes was determined during wind tunnel testing and the exact placements were replicated in CFD. There are 6 locations (placements) of the wake rake for the sphere and wing respectively. Location 1 was located at the center for the sphere and the furthest point away from the wing tip, Figure 6.11. Probe 1 is the uppermost "dot" for each "line" of probes. Only total pressure was measured because the process is adiabatic therefore there is no change in temperature. The absolute total pressure measured was raw data and needs to be corrected. Based on A. Pope [Ref. 55] the data needed to be corrected for solid blockage.

6.2.1 Correction Factors

Solid blockage was due to wind tunnel walls that confine the flow around the model. This reduces the area through which air must flow as compared to free-air conditions and hence, by continuity and Bernoulli's equation, the model saw an increased airflow velocity. The correction factor [Ref. 55] is given by equation (6.1), which is Thom's [Ref 57] short-form equation for solid blockage for a three-dimensional body.

$$\varepsilon_{sb} = \frac{K(\text{Model Volume})}{C^{\frac{3}{2}}} \tag{6.1}$$

Where 'K' equals 0.90 for a 3D wing and 0.96 for a body of revolution and 'C' is the test-section area. According to equation (6.1) the sphere saw a 0.0582% higher velocity and the wing saw a 0.0569% higher velocity. This means that absolute total pressure measured by the wake rake is less than the actual total pressure due to increase in velocity. The next step is to determine uncertainty of the measurements.

6.2.2   Uncertainty

Uncertainty determines the ± error of the measurement. This was based on the pressure sensor accuracy and standard deviation of the collected data per probe. The combined uncertainty was based on the following equation.

$$U_x = \sqrt{U_{x,\text{Instrument}}^2 + U_{x,\text{Std Dev}}^2} \tag{6.2}$$

The uncertainty of the pressure sensor is due to the accuracy given by its operating manual [Ref. 56]. Uncertainty of the sample data is determined by finding the standard deviation, and applying a 95% confidence level to the value [Ref. 55].

6.3 Comparison of Total Pressure between CFD and Wind Tunnel

This section shows the comparison of total pressure between CFD and wind tunnel results. The results also present the corrected total pressure data with its uncertainties. Figure 6.12 to Figure 6.14 displays the area where the sphere and wing were validated between CFD and wind tunnel measurements.
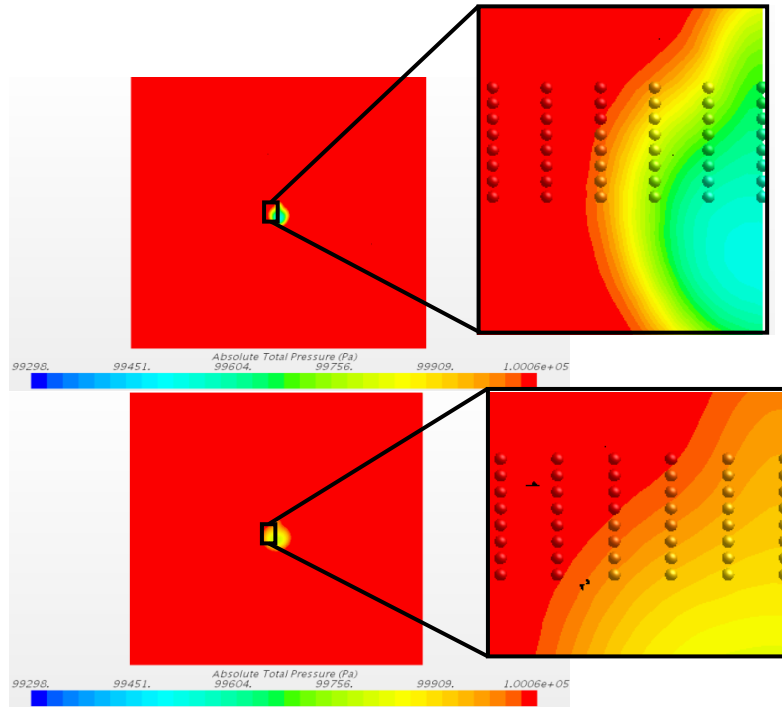
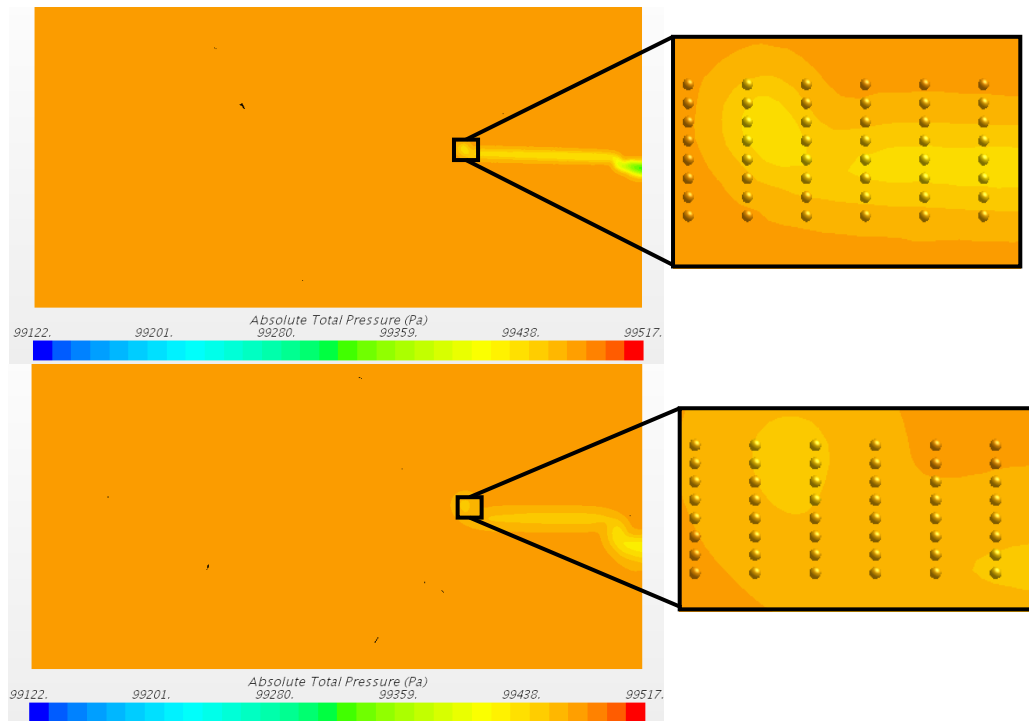**Figure 6.12: Total Pressure Area Validation for the Sphere**

Figure 6.13: Total Pressure Area Validation for the Wing [0 degrees AOA]
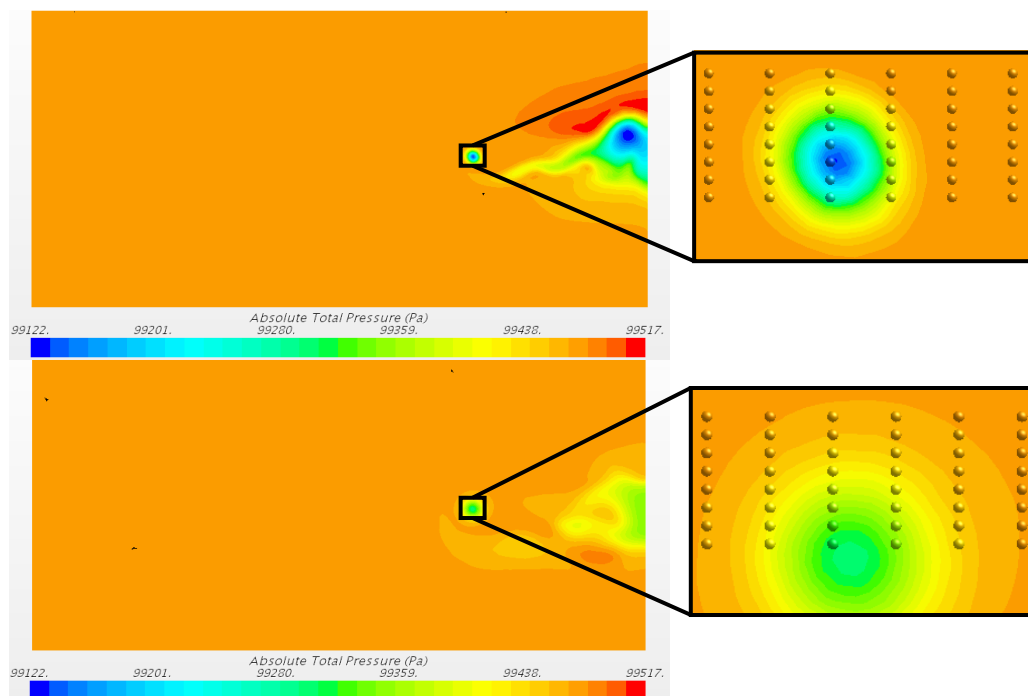

Figure 6.14: Total Pressure Area Validation for the Wing [16 degrees AOA]

6.3.1 <u>1.05D distance away from the Trailing Edge [Sphere]</u>

Figure 6.15 displays the total pressure between wind tunnel and CFD of the sphere. It is observed from the figure that the wind tunnel measurements agree with CFD data at each location. The small

discrepancies exhibited in the figure, location 1: probes 1 to 3, vary in pressure less than 200 Pa. This is considered to be very small, a 0.22% difference.
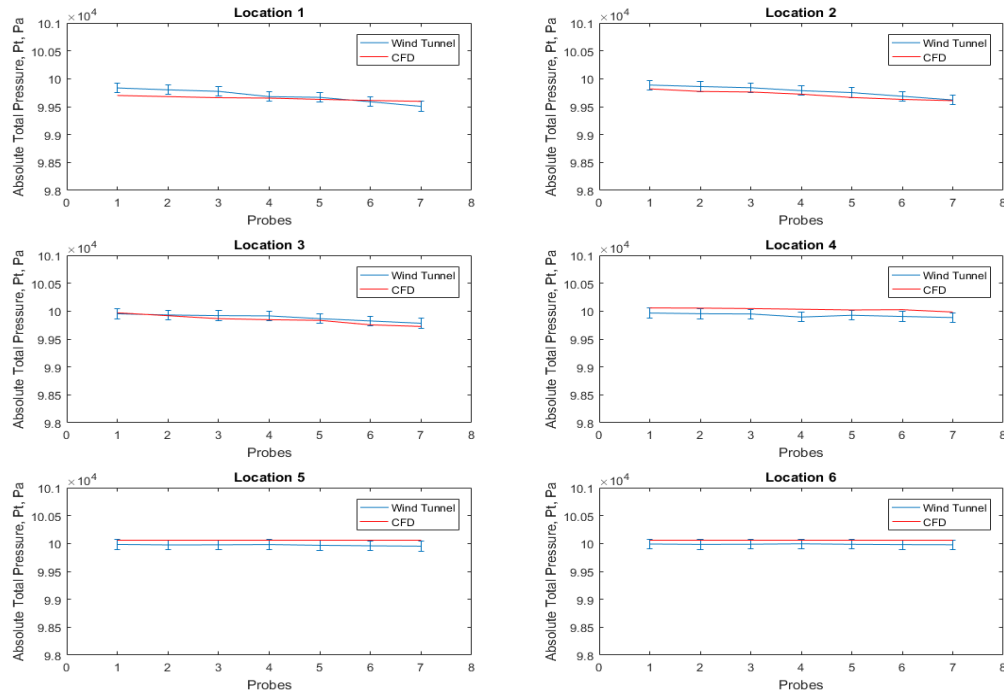
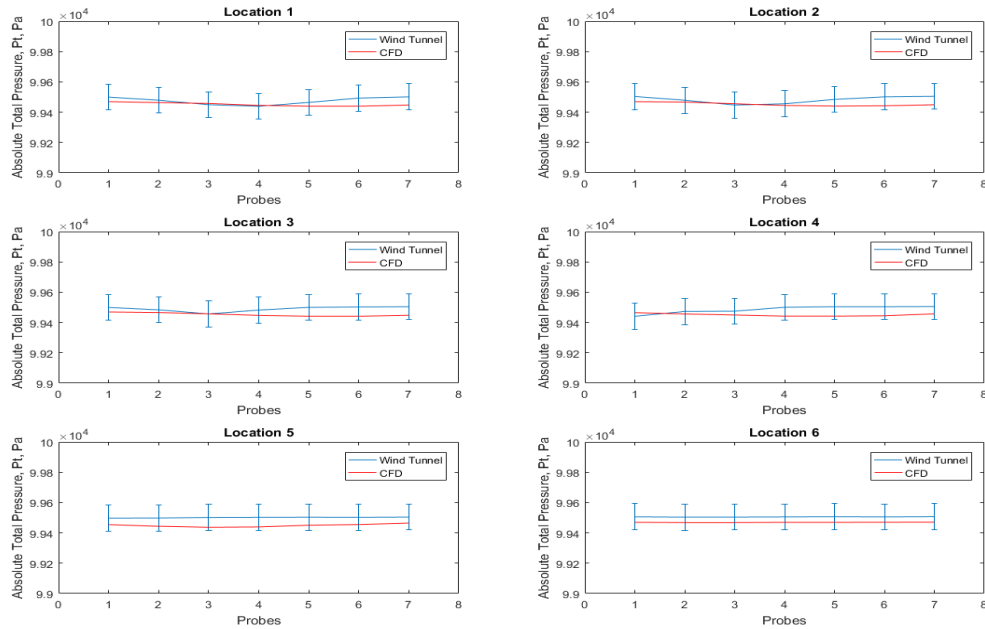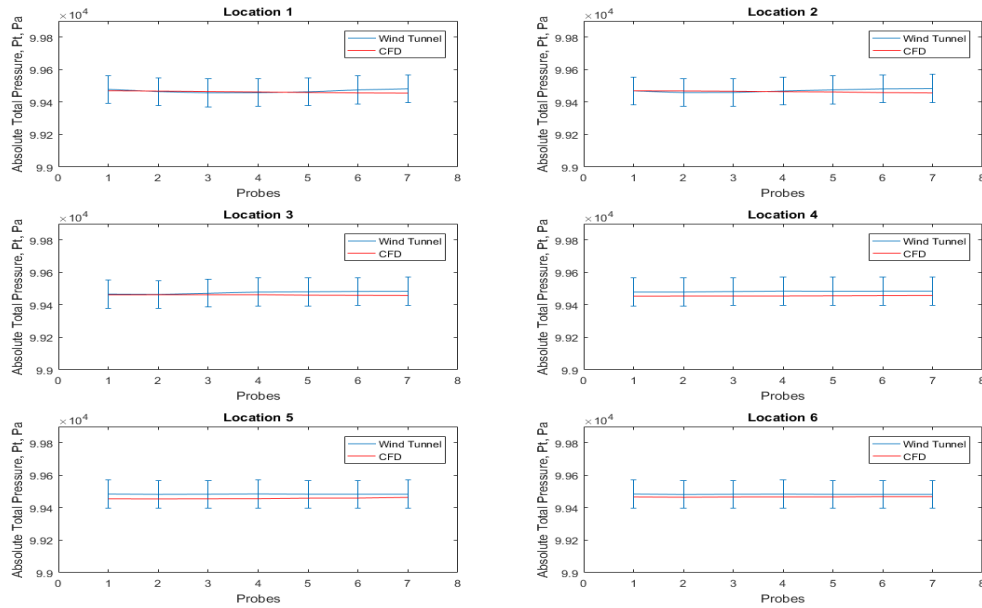**Figure 6.15: Wind Tunnel vs CFD Absolute Pressure Corresponding to Probe Location [Sphere]**

6.3.2   6D distance away from the Trailing Edge [Sphere]

From Figure 6.16 it can be observed that the wind tunnel total pressure measurement is lower than CFD. The average difference for each location is less than 0.25%, therefore the comparison is considered to be in good agreement.
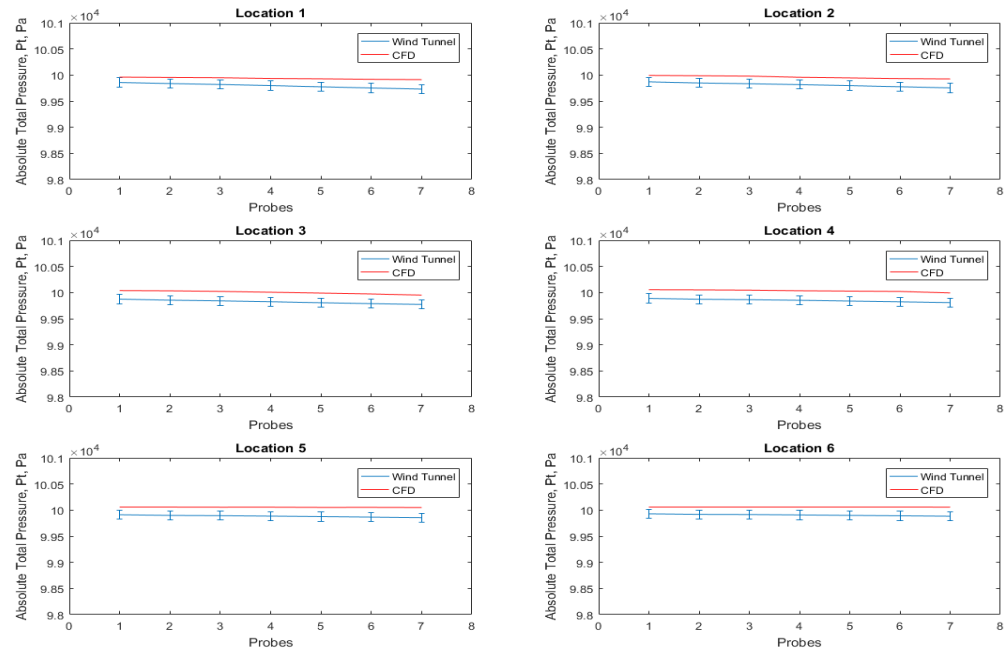
Figure 6.16: Wind Tunnel vs CFD Absolute Total Pressure Corresponding to Probe Location [Sphere]

46

6.3.3   1.05D distance away from the Trailing Edge [Wing – 0 degrees AOA]

Figure 6.17 exhibits that the total pressure between CFD and wind tunnel agree with each other, where the CFD data curve is within the uncertainty of the wind tunnel measurements.

Figure 6.17: Wind Tunnel vs CFD Absolute Total Pressure Corresponding to Probe Location [Wing – 0 degrees AOA]

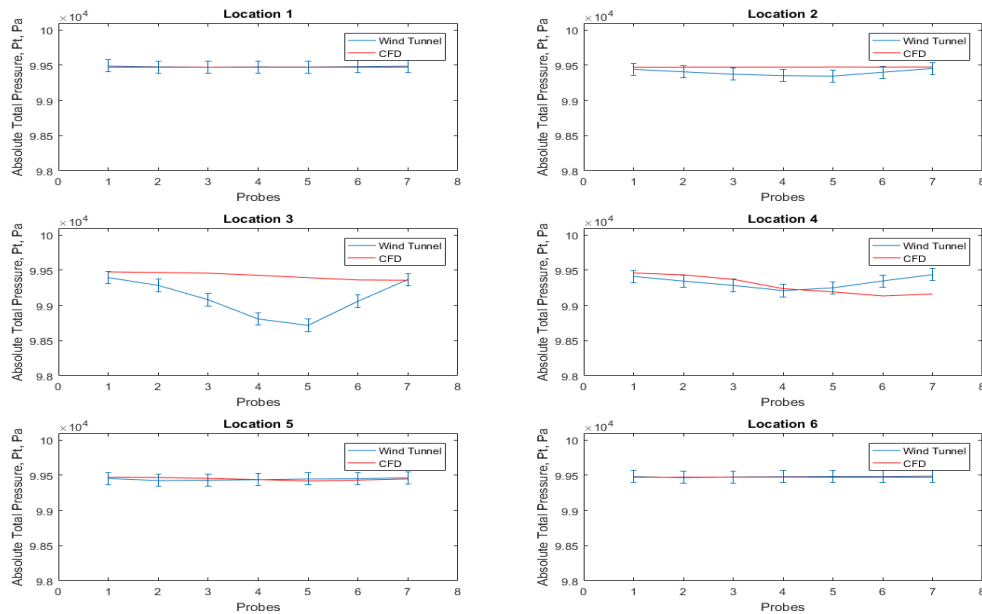### 6.3.4   6D distance away from the Trailing Edge [Wing – 0 degrees AOA]

At a further distance away from the trailing edge of the wing. The total pressure measurement between CFD and wind tunnel data are in good agreement, Figure 6.18. As observed in the figure, the CFD data line is within the uncertainty range of wind tunnel measurements.

Figure 6.18: Wind Tunnel vs CFD Absolute Total Pressure Corresponding to Probe Location [Wing – 0 degrees AOA]

6.3.5 1.05D distance away from the Trailing Edge [Wing – 16 degrees AOA]

Figure 6.19 exhibit that CFD and wind tunnel agree for total pressure except at locations 2 to 4. These discrepancies can observed at location 2 between probes 3 and 6, location 3 between probes 2 and 6, and location 4 between probes 6 and 7. The difference between CFD and wind tunnel total pressure is due to the vortex and separated flow, which is exhibited in Figure 6.14. It is difficult to capture the wake disturbance, since the pitot tubes need to be aligned with the local flow.

Figure 6.19: Wind Tunnel vs CFD Absolute Total Pressure Corresponding to Probe Location [Wing – 16 degrees AOA]

6.3.6   6D distance away from the Trailing Edge [Wing – 16 degrees AOA]

As observed at the closet distance to the wing, the same trend holds further away from the model. The data is not in good agreement between CFD and wind tunnel, at location 2 through 4 which can be observed in Figure 6.20. The change is evident at location 2 and 4 between probes 3 and 7. The same hypotheses hold, that the pitot tubes of the wake rake were not aligned with the local flow. Since these locations are within the vortex, as exhibited in Figure 6.14, it is very difficult to accurately capture this disturbance.
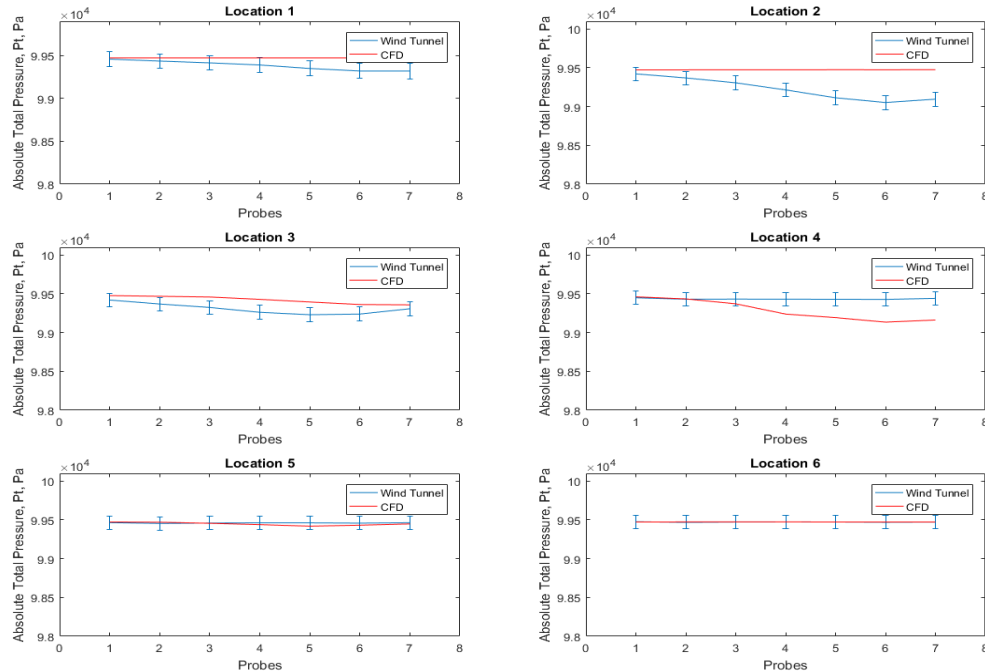
Figure 6.20: Wind Tunnel vs CFD Absolute Total Pressure Corresponding to Probe Location [Wing – 16 degrees AOA]

6.4 CFD Entropy Signature of the Sphere and Wing

CFD entropy signatures generated are displayed in Figure 6.21 to Figure 6.30. The entropy signature map for the sphere and wing follow the same trend as their corresponding total pressure. The strongest signature, for the sphere and wing, was recorded closest to the model, which then dissipates downstream. The wing maintains the same signature from 0 to 12 degrees, but varies after 12 degrees since that is when the wing stalls.
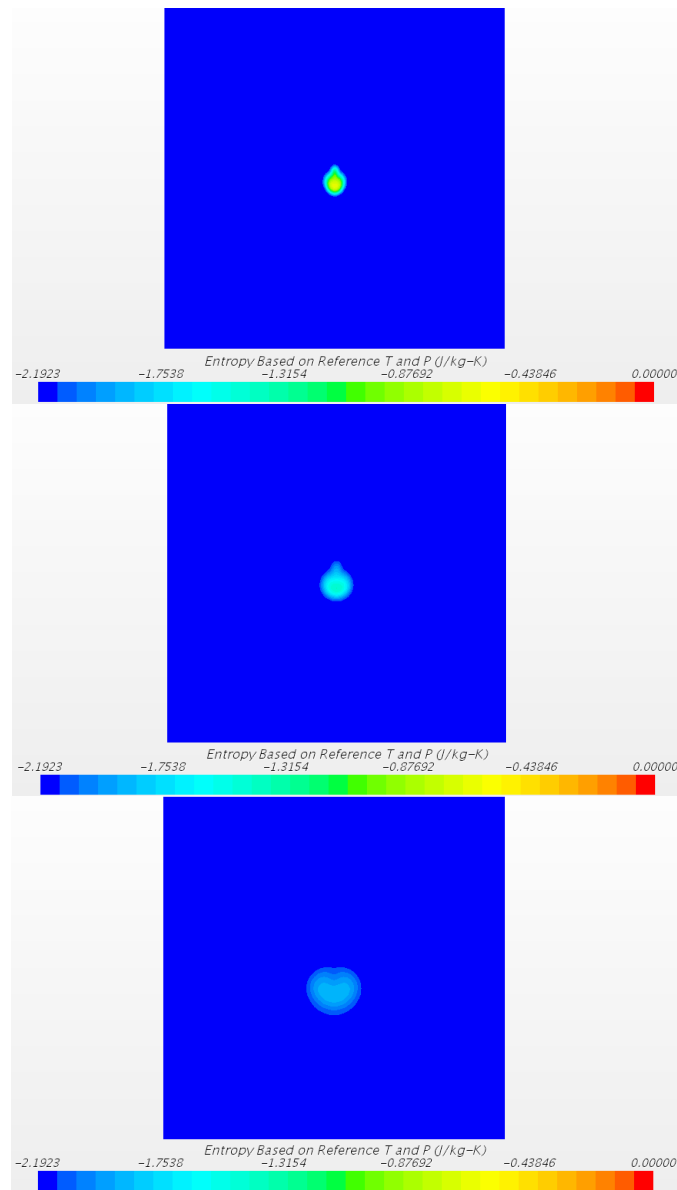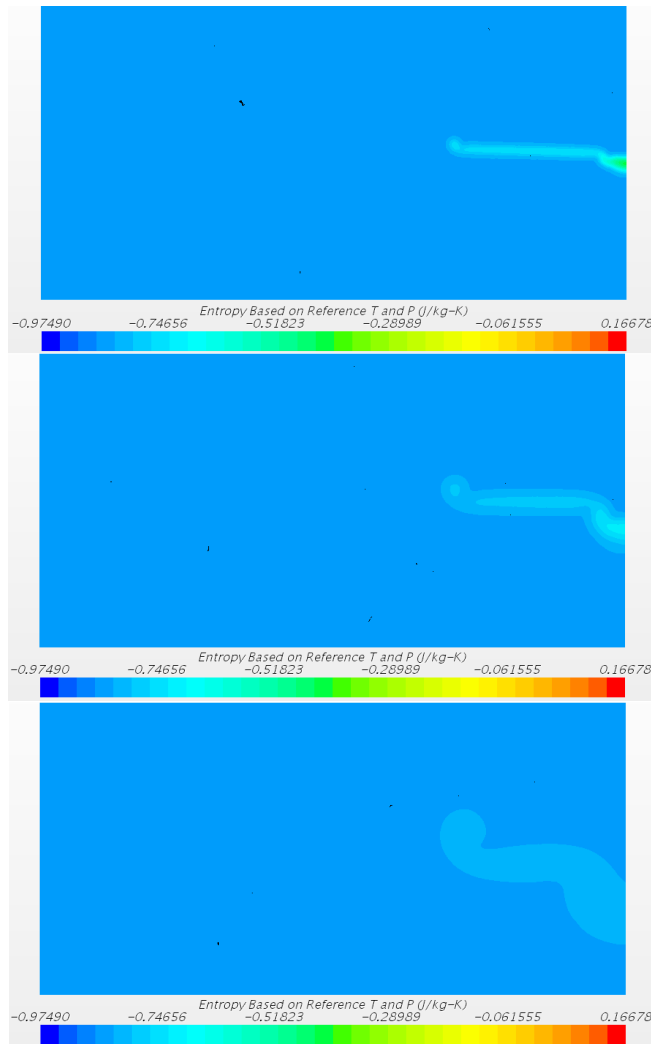
Figure 6.21: Sphere Entropy Signature
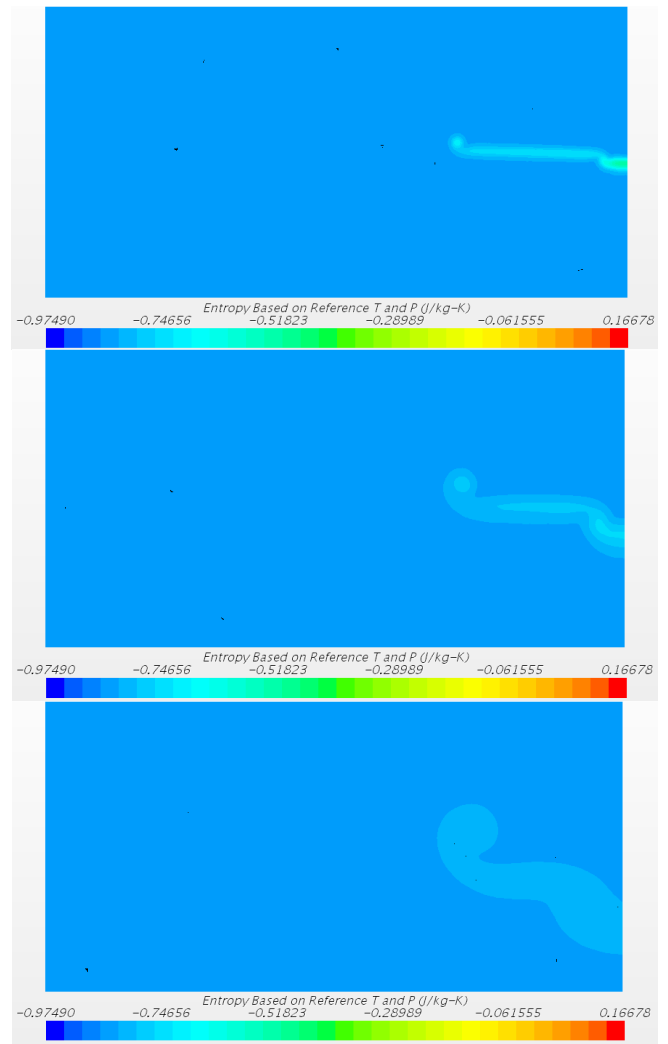
Figure 6.22: Wing Entropy Signature [0 deg]

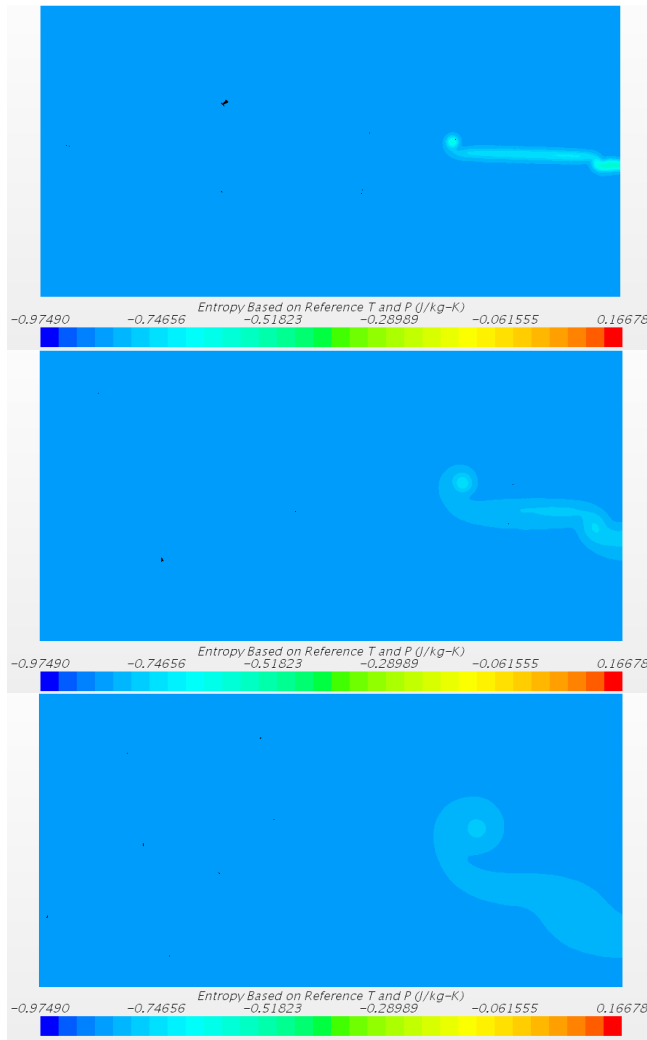**Figure 6.23: Wing Entropy Signature [2 deg]**

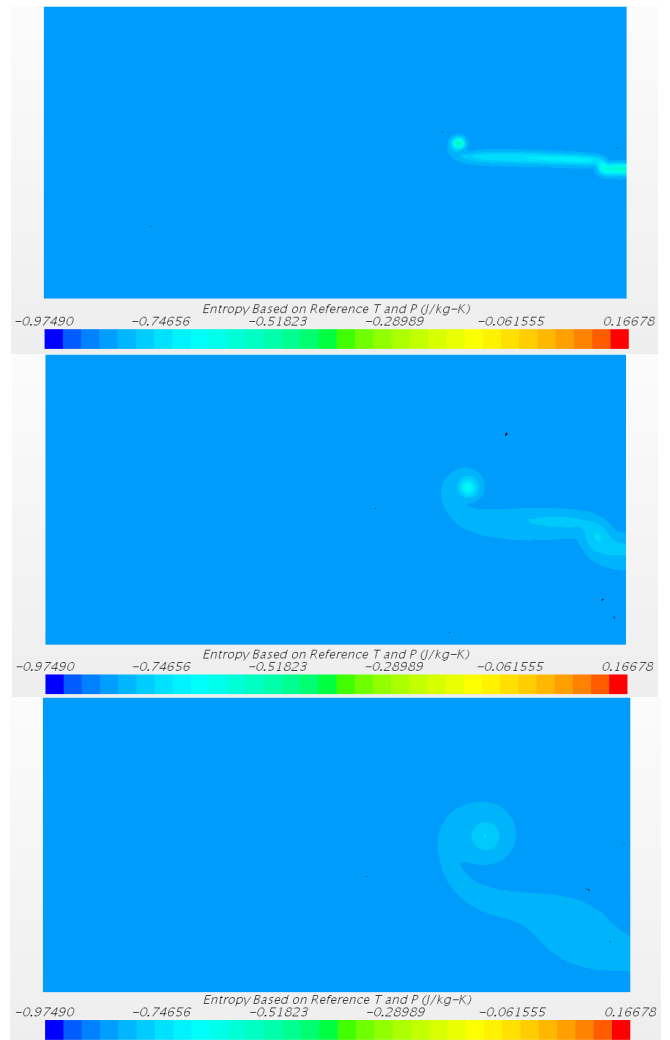**Figure 6.24: Wing Entropy Signature [4 deg]**

Figure 6.25: Wing Entropy Signature [6 deg]
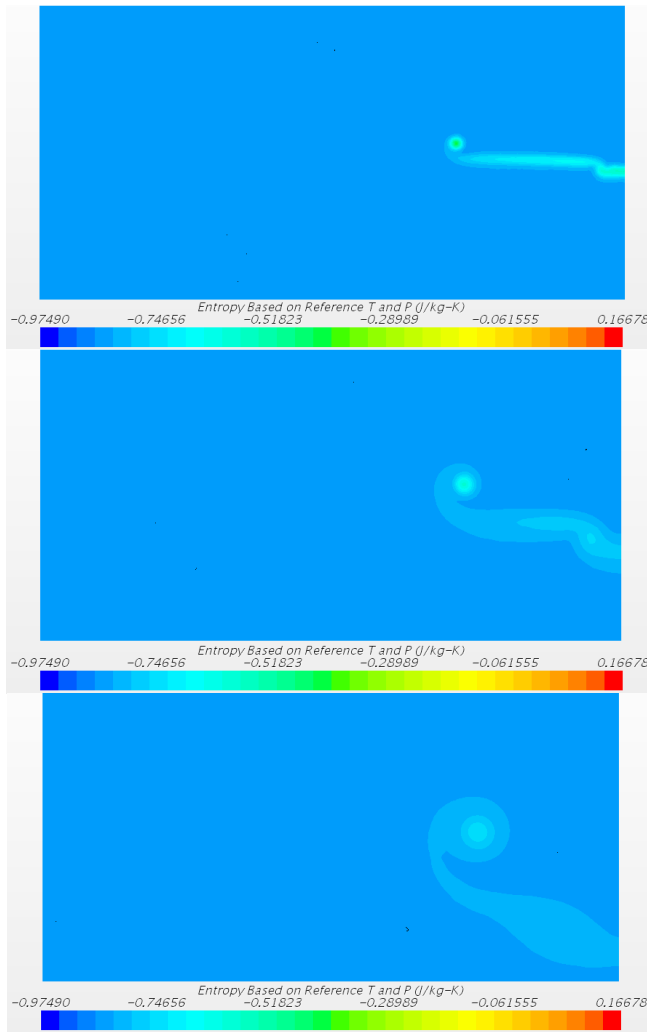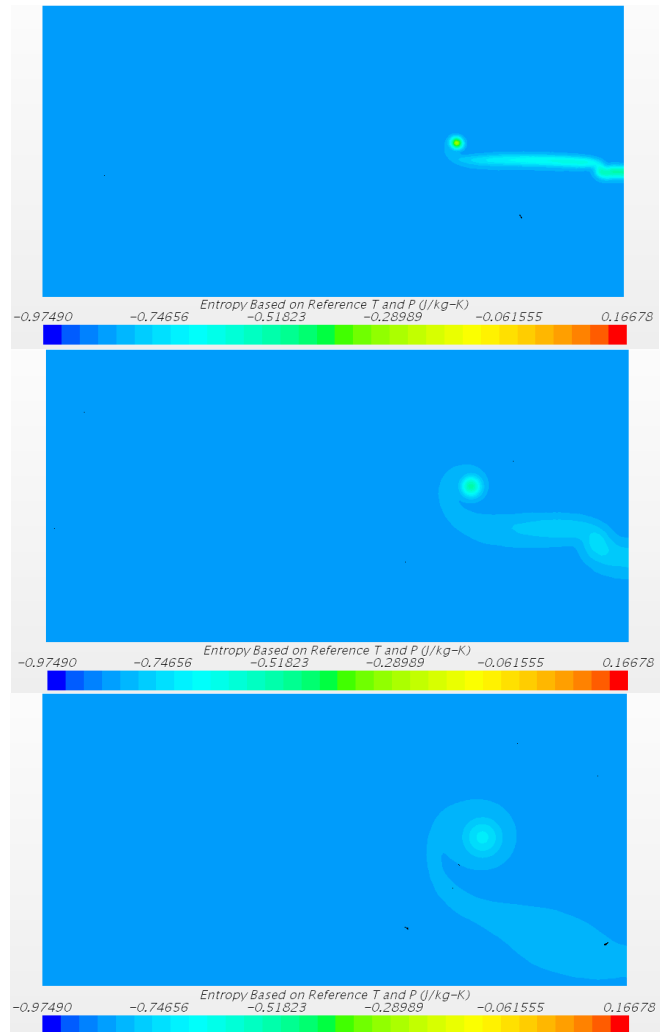
Figure 6.26: Wing Entropy Signature [8 deg]
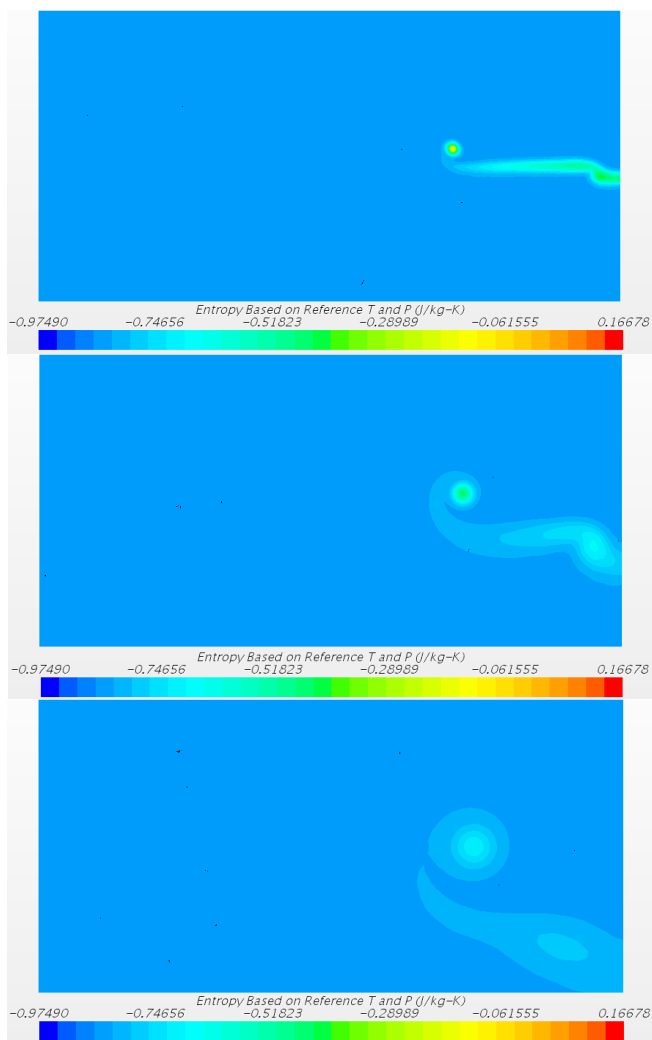

Figure 6.27: Wing Entropy Signature [10 deg]

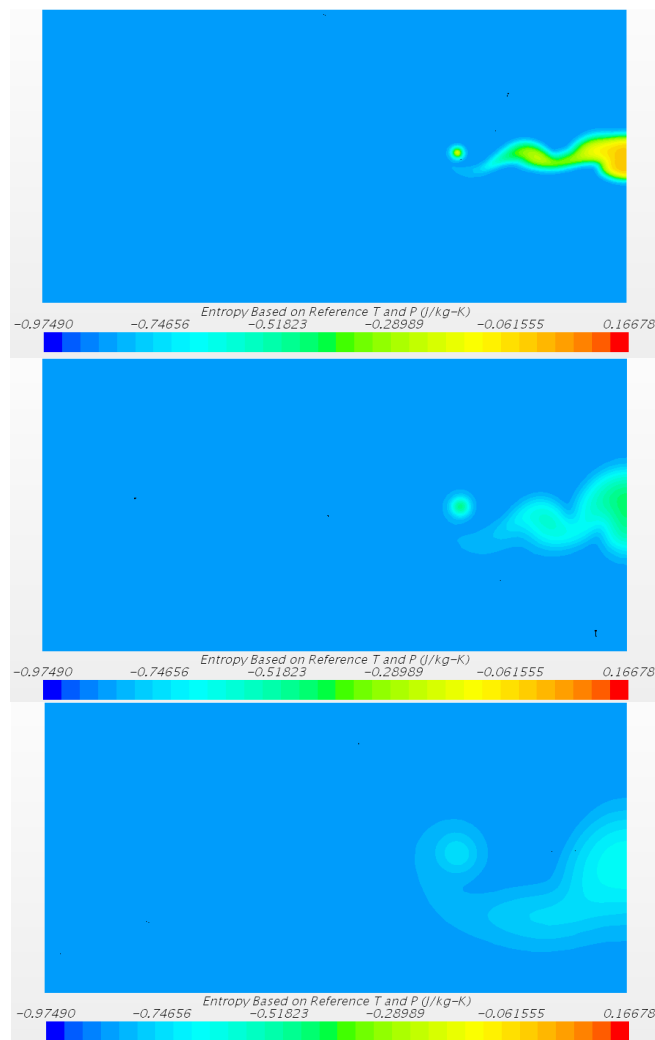**Figure 6.28: Wing Entropy Signature [12 deg]**

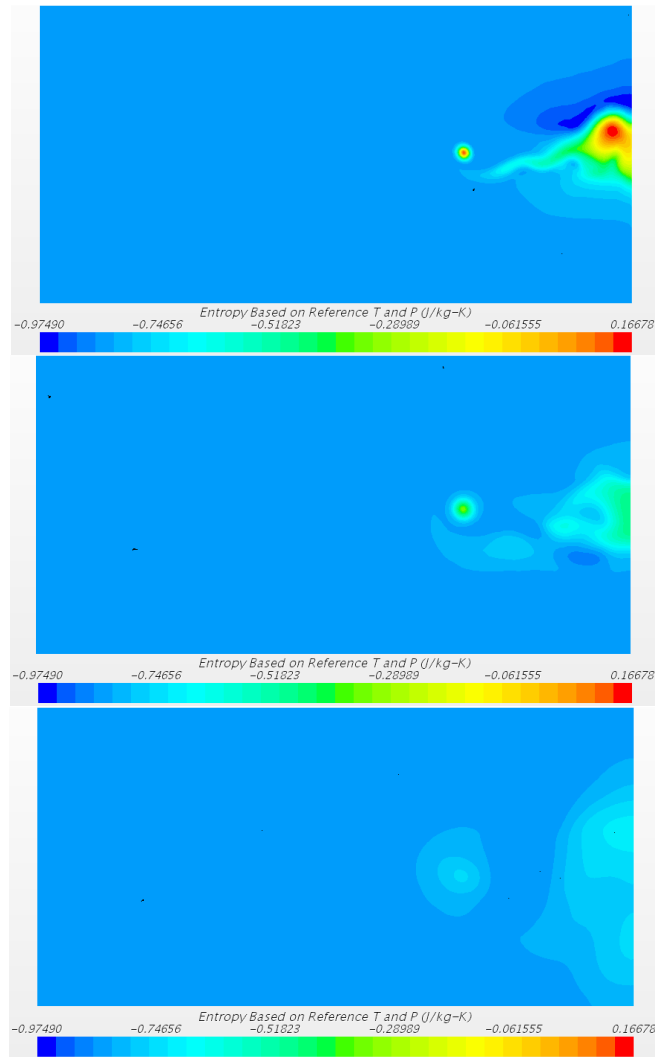**Figure 6.29: Wing Entropy Signature [14 deg]**

Figure 6.30: Wing Entropy Signature [16 deg]

6.5 Comparison of Entropy Signature between CFD and Wind tunnel

This section displays that the sphere and wing entropy signature. Figure 6.31 to Figure 6.33 displays the area where the sphere and wing were validated between CFD and wind tunnel measurements. It is also noted, since entropy measured was based on pressure, that the same discrepancies exhibited for the total pressure comparison will also be observed for the entropy comparison.
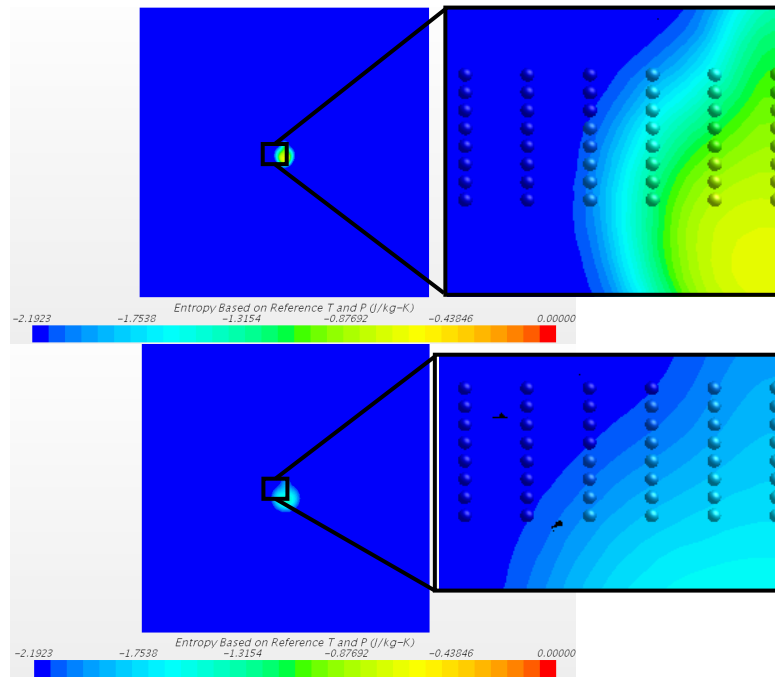

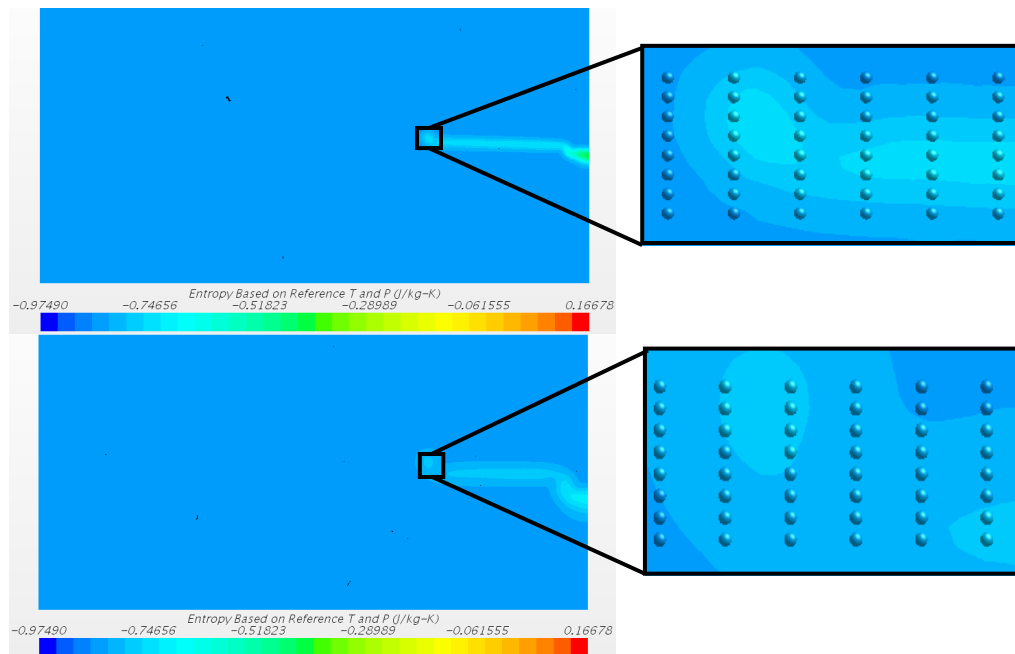
Figure 6.31: Entropy Area Validation of the Sphere

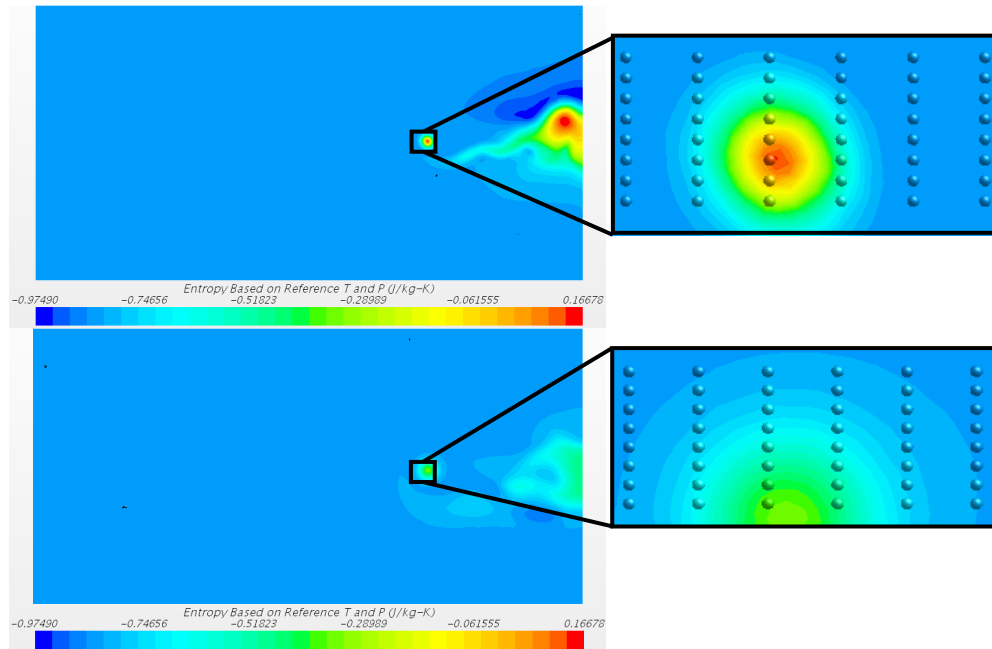**Figure 6.32: Entropy Area Validation of the Wing [0 degrees AOA]**

Figure 6.33: Entropy Area Validation for the Wing [16 degrees AOA]

6.5.1   1.05D distance away from the trailing edge [Sphere]

Sphere entropy trail can be observed in Figure 6.34. The figure exhibits entropy variations at the most inboard location and then levels off towards the outboard location for the sphere. Discrepancies in measured values are at the same location as observed for total pressure differences between CFD and wind tunnel. This makes sense since entropy calculated is based on absolute pressure measurements.
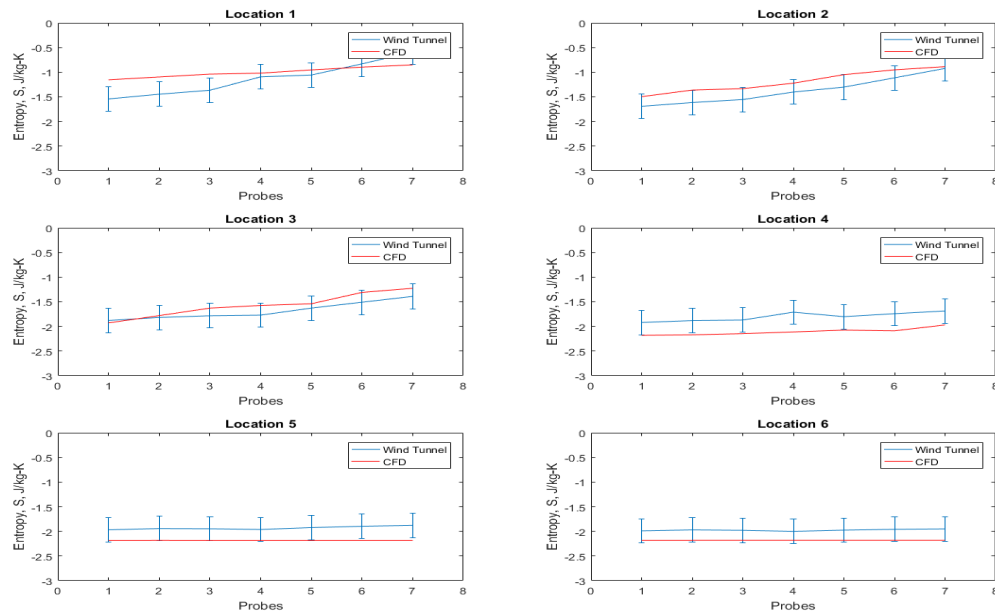

Figure 6.34: Wind tunnel v CFD Entropy corresponding to probe location [Sphere]

6.5.2   6D distance away from the trailing edge [Sphere]

Figure 6.35 exhibits the entropy trail comparison further away from the sphere. Again the difference between CFD and wind tunnel measurements is due to the difference in absolute pressure measured.
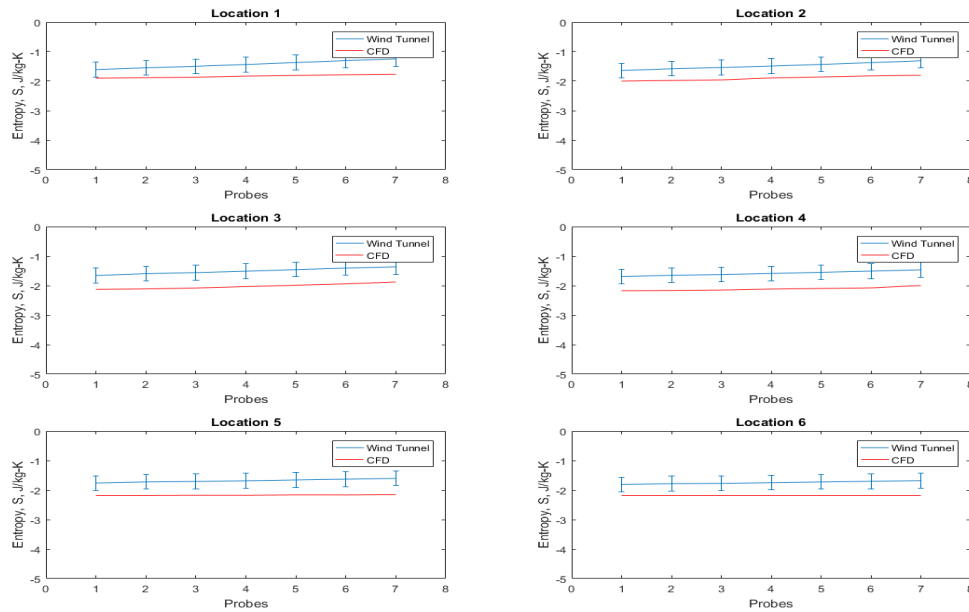
Figure 6.35: Wind tunnel v CFD Entropy corresponding to probe location [Sphere]

6.5.3   1.05D distance away from the trailing edge [Wing – 0 degrees AOA]

Figure 6.36 displays the entropy measured between CFD and wind tunnel are in good agreement with each other. It can be observed from the figure that the entropy is relatively constant at each location.

Figure 6.36: Wind tunnel v CFD Entropy corresponding to probe location [Wing – 0 degrees AOA]

6.5.4   6D distance away from the trailing edge [Wing – 0 degrees AOA]

The same trend exhibited closest to the wing can be observed further downstream. The entropy measurement is relatively constant and is in good agreement between CFD and wind tunnel measurements.
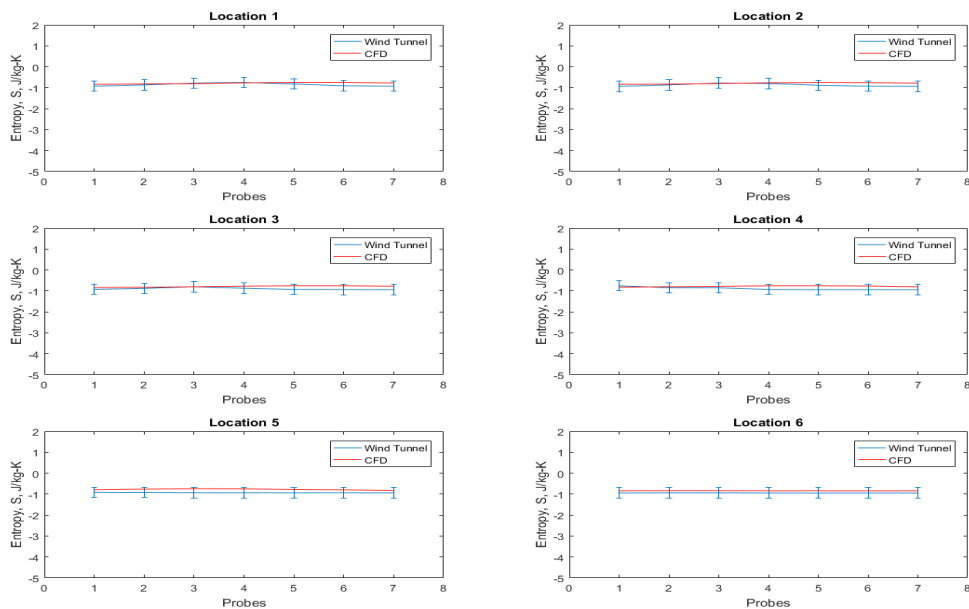

Figure 6.37: Wind tunnel v CFD Entropy corresponding to probe location [Wing – 0 degrees AOA]

6.5.5   1.05D distance away from the trailing edge [Wing – 16 degrees AOA]

At 16 degrees AOA, the wing exhibits relatively constant entropy values at each location except for location 3 and 4. The difference between CFD and wind tunnel recordings are due to the vortex and separated flow. Since the absolute pressure measurements was not able to capture the vortex, the difference affects the entropy measurement, which can be observed in Figure 6.38.
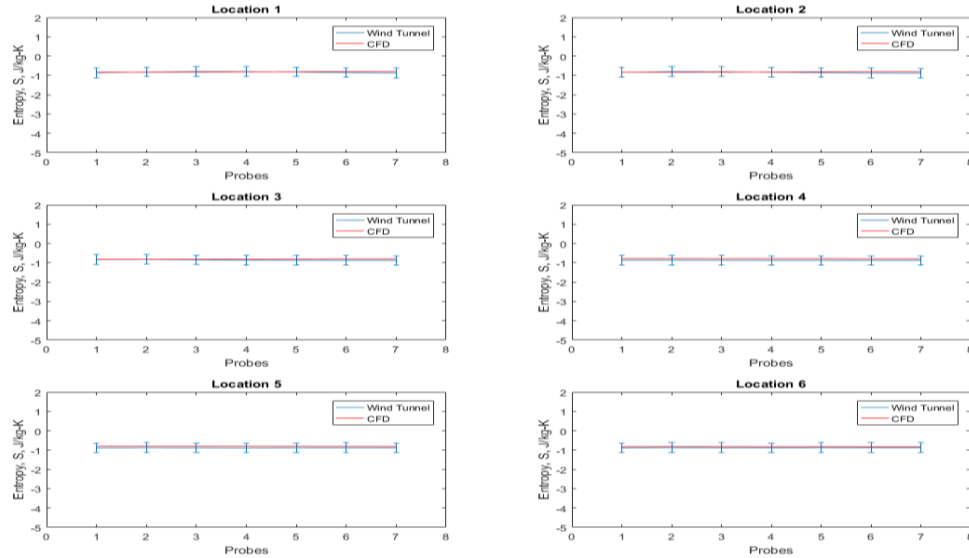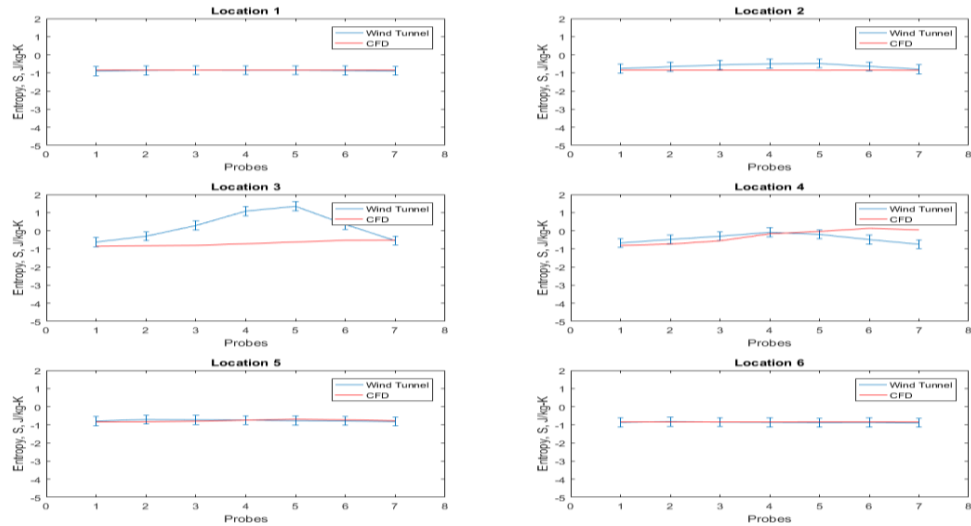
Figure 6.38: Wind tunnel v CFD Entropy corresponding to probe location [Wing – 16 degrees AOA]

6.5.6   6D distance away from the trailing edge [Wing – 16 degrees AOA]

Just as exhibited at the closest location to the wing. The difference between CFD and wind tunnel entropy, further downstream, is due to the presence of the vortex as exhibited in Figure 6.33. The wind tunnel measurements could not capture the vortex and separated flow since the probes were not aligned with the local flow.

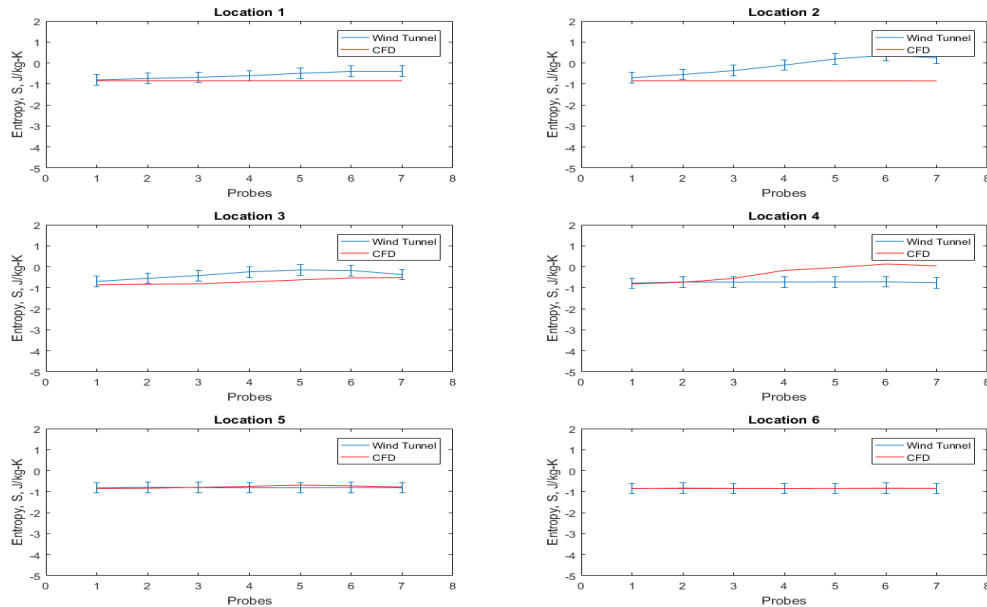**Figure 6.39: Wind tunnel v CFD Entropy corresponding to probe location [Wing – 16 degrees AOA]**

60

7   <u>Conclusion</u>

Based on literature review, infrared, radar, and noise are the three main aircraft signatures. The sphere and wing exhibited negligible signatures. The IR signature was reliant on aerodynamic heating, where the difference between airframe temperature and ambient temperature was 0.18% and 0.07% of the sphere and wing, respectively. For radar signature the RCS was -19.9 dBm^2 and -10.6dBm^2, sphere and wing, respectively. Noise generation was negligible since the flow Mach number was less than 0.1 and noise generation is proportional to the incoming flow velocity. With the use of low observable technology, these signatures can be reduced dramatically. This is where the new observable, entropy trail, is introduced. Based on the 2nd Law of Thermodynamics and Gibbs equation, any object regardless of shape, size, and low observable technology when in motion will generate a unique entropy trail.

It was evident that the sphere and wing produced an entropy wake, which was successfully recorded. This was exhibited in CFD and wind tunnel results. Both results were in good agreement with each other with discrepancies in absolute total pressure and entropy for the wing at 16 degrees AOA. This discrepancy was due to the presence of a vortex and separated flow, which the wind tunnel measurements could not capture.

8   <u>Recommendation for Future Work</u>

Since wind tunnel measurements were not able to capture the vortex and separated flow the use of a hot wire instead of a pitot tube would be advised. Another recommendation is to investigate the entropy trail of the wing and sphere in tandem. Subtract the sphere entropy trail with the total trail and observe if the wing entropy trail is the remainder. Another study would be to determine the entropy signature of existing aircraft, by mapping out their generated 3D wake. The end goal is to build a database to identify aircraft based on their unique entropy trail signature. The last recommendation is to determine a way to measure entropy change in real time.

References

1. Farokhi, S., Taghavi, R.R., and Keshmiri, S.S., *"On Entropy Trail"*, 68th Annual Meeting of APS-DFD, Boston, MA, 2015.

2. Sweetman, B., *"Stealth Aircraft"*, Motorbooks International, Osceola, WI, 1986.

3. Ball, R.E., *"The fundamentals of Aircraft Combat Survivability Analysis and Design"*, 2nd Edition, AIAA Education Series, Reston, VA, 2003.

4. Jenn, D.C., *"Radar and Laser Cross Section Engineering"*, AIAA Education Series, Reston, VA 1995.

5. Muller, I., and Weiss, W., *"Entropy and Energy,"* Springer, NY, 2005

6. Farokhi, S., *"Aircraft Propulsion"*, 2nd Edition, John Wiley and Sons, Ltd. Chichester (UK), 2014.

7. Jack, W.R., *"Aircraft Infrared Principles, Signatures, Threats, and Countermeasures,"* Naval Air Warfare Center Weapons Division Point Mugu, CA, September 2012

8. Naval Air Warfare Center, *"Electronic Warfare and Radar Systems Engineering Handbook,"* Avionics Department AIR-4.5, Washington, DC, April 1999

9. FLIR Research and Science, *"FLIR Infrared Systems for Research and Science,"* 2017

10. Shripad, M.P., Hemant, S.R., and Arvind, R.G., *"Infrared Signature Studies of Aerospace Vehicles,"* Department of Aerospace Engineering, IIT, Bombay, India

11. Zhang, J., Pan, C., and Shan, Y., *"Progress in Helicopter Infrared Signature Suppression,"* Chinese Journal of Aeronautics, 2014

12. Krishnamorth, V., Pai, B.R., *"Aerothermodynamics and Infrared Emission Characteristics of Simulated Aeroengine Jet Plumes,"* National Aerospace Laboratories, Bangalore, India, July 1991

13. Wu, C., Farokhi, S., and Taghavi, R., *"Computational Study of Advanced Exhaust System Transition Ducts with Experimental Validation,"* J Propulsion Power, 1993

14. MIKRON, "Table of Emissivity of Various Surfaces for Infrared Thermometry," Mikron Instrument Company, Inc.

15. Thompson, J., Gubbels, A.W., Barry, B., and Birk, A.M., *"Design of an Infrared Signature Suppression for the Bell 205 Helicopter, Part II Engine and Flight Testing,"* 11th CASI Aerodynamics Symposium, 2001

16. Thompson J., Birk A.M., and Cunningham M., *"Design of infrared signature suppressor for the Bell 205 (UH-1H) Helicopters,"* Part I: aerothermal design. Proceedings of Seventh CASI propulsion symposium, 1999

17. Thompson J., Gubbels A.W., and Barry B, et al., *"Design of an infrared signature suppression for the Bell 205 (UH-1H) Helicopter,"* Part-II: engine & flight testing[C]. Proceedings of 11th CASI Aerodynamics Symposium, 2001

18. Dix, J., Saddington, A.J., Knowles, K., and Richardson, M.A., *"Infrared signature reduction study on a small-scale jet engine,"* Aeronaut J 2005;109(1092):83–8

19. Yan, H., Xiong, Z., and Jian, G., *"Preparation and Properties of EPDM-Based Composite Coatings with Low Infrared Emissivity,"* J. Energy Eng, 2016, 142(4); -1-1

20. DeSteese, J.G., Antoniak, Z.I., White, M., Peters, T.J., *"Structure and method for controlling the thermal emissivity of a radiating object,"* US Patent no. 6713774 B2, March 30, 2004

21. Conway, T.G., McClean, R.G., and Walker, G.W., *"Three color infrared camouflage system,"* US Patent no. 5077101, December 31, 1991

22. Miacci, M.A.S., and Rezende, M.C., *"Basics on Radar Cross Section Reduction Measurements of Simple and Complex Targets Using Microwave Absorbers,"* InTech, February 24th, 2012

23. Singh, H., and Jha, R.M., *"Active Radar Cross Section Reduction: Theory and Applications,"* Cambridge University Press

24. Brooker, G., *"Introduction to Sensors for Ranging and Imaging,"* Target and Clutter Characteristics, 2009

25. Yuan, H.W., Wang, X., Gong, S.X., and Zhang, P., *"A Numerical Method For Analyzing the RCS of a printed Dipole Antenna with Feed Structure,"* Journal of Electromagnetic Waves and Applications 22: 1661-70

26. Currie, N.C., *"Radar Reflectivity Measurement: Techniques and Applications,"* Academic Press, NY 1989

27. Yuzcelik, C.K., *"Radar Absorbing Material Design,"* Master Thesis, Naval Postgraduate School, CA 2003

28. Hakan, U., *"Radar Cross Section Reduction,"* Journal of Naval Science and Engineering, Vol 9, No. 2, pp 72-87, 2013

29. https://en.wikipedia.org

30. David, C. J., *"Radar and Laser Cross Section Engineering,"* Ohio: AIAA Education Series, 1995

31. Shaeffer, J.F., Tuley, M.T., and Knott, E.F., *"Radar Cross Section,"* SciTech Publishing, 2004.

32. Leylekian, L., Lebrun, M., and Lempereur, P., *"An Overview of Aircraft Noise Reduction Technologies,"* Aerospace Lab Journal, Issue 7, June 2014.

33. Enghardt, L., *"Improvement of Fan Broadband Noise Prediction: Experimental Investigation and Computational Modeling,"* Proband, CEAS Broadband Noise Workshop Bilbao, 2008.

34. Bamberger, K., and Carolus, T., *"Optimization of Axial Fans with Highly Swept blades with respect to Losses and Noise Reduction,"* University of Siegen, Germany, 2012.

35. Mardjono, J., Riou, G., Boiteux, J.M., and Boubila, F., *"Static Tests Demonstration of Liners Noise Reduction Concepts,"* EPSL, AIAA 2013-2174.

36. Shigeo, H., Roy, M.Y., Mark. D.R.D., and Ed, W., *"Determining the Entropy Generated in a Low Reynolds Number Compressor Cascade Based on the wake Velocity profile,"* AIAA Paper 06-7810, Sept. 2006.

37. Denton, J.D., 1993, *"Loss Mechanisms in Turbomachines,"* Journal of Turbomachinery, Vol. 115, pp. 621-656.

38. Davies, M.R.D. and O'Donnell, F.K., 1999, *"Local Measurement of Loss using Heated Thin Film Sensors,"* ASME Journal of Turbomachinery, Vol. 121, pp. 814-818.

39. Davies, M.R.D., O'Donnell, F.K., and Niven, A.J., *"Turbine Blade Entropy Generation Rate Part I: The Boundary Layer Defined,"* ASME Paper 2000-GT-0265, ASME Turbo Expo, Munich, Germany.

40. O'Donnell, F.K. and Davies, M.R.D., *"Turbine Blade Entropy Generation Rate Part II: The Measured Loss,"* ASME Paper 2000-GT-0266, ASME Turbo Expo, Munich, Germany.

41. Michel, M., Ndaona, C., Anestis, K.I., and Reza, A.S., *"Time-resolved entropy measurements using fast response entropy probe,"* Measurement Science and Technology, Sept. 2008.

42. Payne, S. J., Ainsworth, R. W., Miller, R. J., Moss, R. W., and Harvey, N. W., *"Unsteady loss in a high pressure turbine stage,"* International Journal of Heat and Fluid Flow, 24 (2003) 698-708

43. Anderson, J., *"Fundamentals of Aerodynamics"*, 6th Edition, Mc Graw Hill

44. CD-Adapco, STAR-CCM+ [http://www.cd-adapco.com]

45. CD-Adapco, STAR-CCM+, Manual, 2016

46. Constantinescu. G., Chapelet. M., and Squires, K., *"Turbulence Modeling Applied to Flow over a Sphere,"* Arizona State University, Tempe, AZ, AIAA Journal, Vol. 41, No.9, September 2003

47. Chen, H.C., and Patel, V.C., *"Near-wall Turbulence Models for Complex Flows Including Seperation,"* AIAA Journal, Vol. 26, 1988, pp. 641-648

48. Wilcox, D.C., *"Reassessment of the Scale-Determining Equation for Advanced Turbulence Models,"* AIAA Journal, Vol. 26, 1988, pp. 1299-1310.

49. Durbin, P.A., *"Near-Wall Turbulence Closure Without Damping Functions,"* Theoretical and Computational Fluid Dynamics, Vol. 3, No.1, 1991, pp. 1-13

50. Spalart, P.R., and Allmaras, S.R., *"A One-Equation Turbulence Model for Aerodynamic Flows,"* La Recherche Aerospatiale, Vol. 1, 1994, pp. 5-21

51. Germano, M., Piomelli, U., Moin, P., and Cabot, W.H., *"A Dynamic Subgrid –Scale Eddy Viscosity Model,"* Physics of Fluids A, Vol. 3, 1991, pp. 1760-1765.

52. Spalart, P.R., Jou, W.H., Strelets, M., and Allmaras, S.R., *"Comments on the Feasibility of LES for Wings, and on Hybrid RAN/LESS Approach,"* Advances in DNS/LES: First AFOSR International Conference on DNS/LES, edited by C. Liu and Z. Liu, Greyden, Columbus, OH, 1997

53. Taghavi, R., *"Lab handout AE 445,"* Spring 2011, Department of Aerospace Engineering, University of Kansas.

54. University of Kansas., *"Laboratory Facilities,"* https://ae.engr.ku.edu/facilities

55. Barlow, B.J., Rae, H.W. Jr, and Pope, A., *"Low-Speed Wind Tunnel Testing,"* 3rd edition, John Wiley and Sons, Inc, NY, 1999

56. NXP, *"MPXV7002 Data Sheet,"* Freescale Semiconductor, Inc, 2015

57. Thom, A., *"Blockage Corrections in a High speed Wind Tunnel,"* ARC R&M 2033, 1943
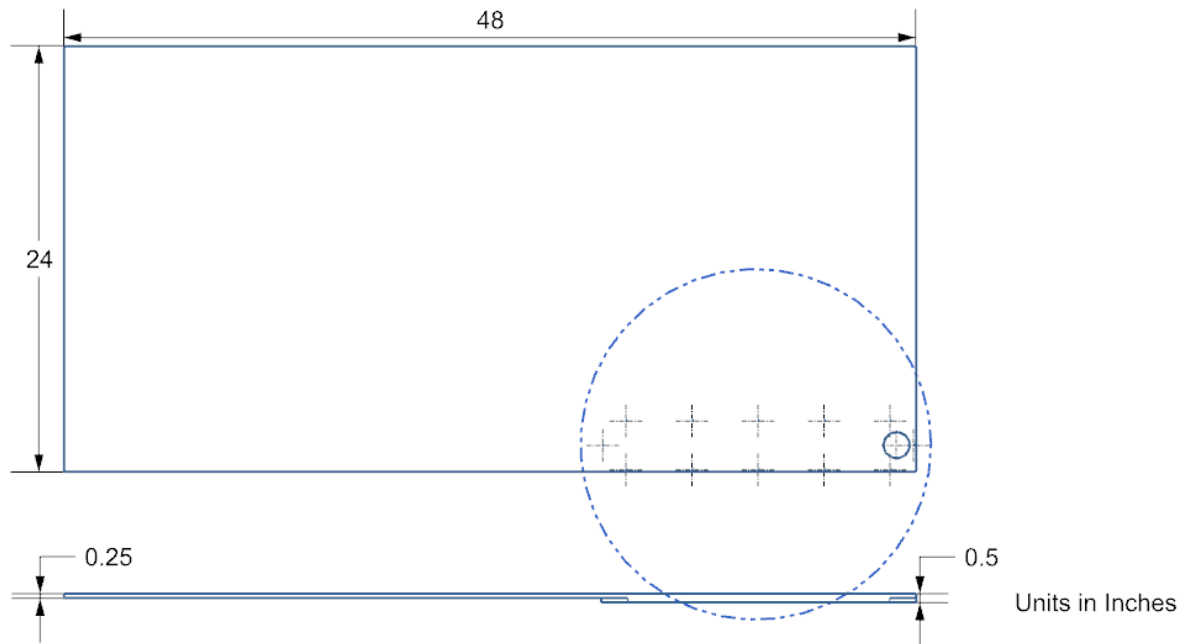
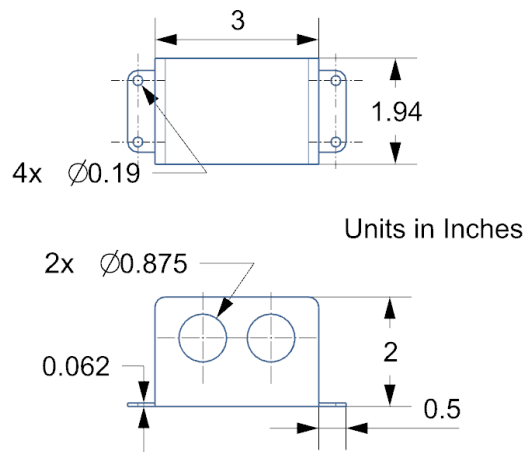## Appendix
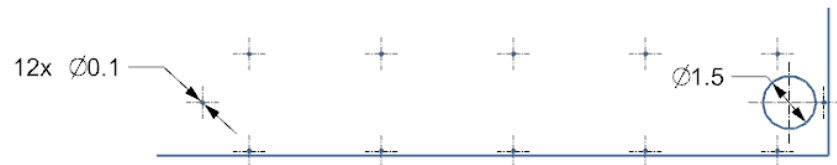
Figure A 1: Test Board Dimension
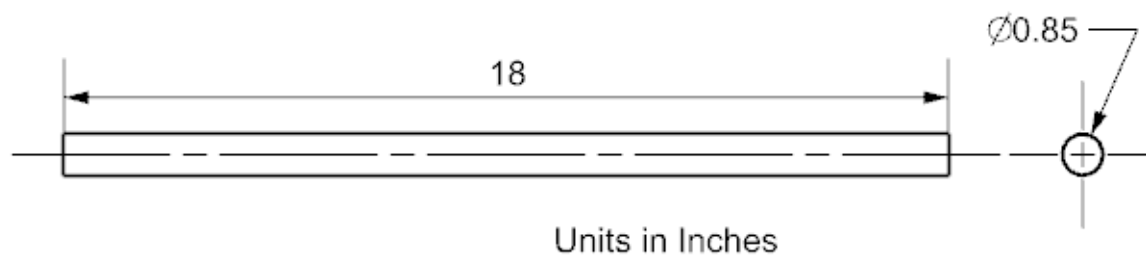

Figure A 2: Slider end point Dimensions

18

Ø0.85

Units in Inches

Figure A 3: Slider Rod Dimension

3   1

2x Ø0.375

5.75

17.75

8.25

Ø0.85
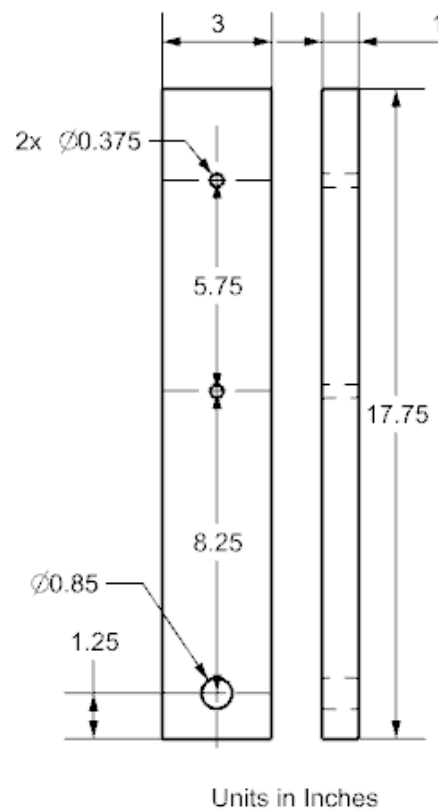
1.25

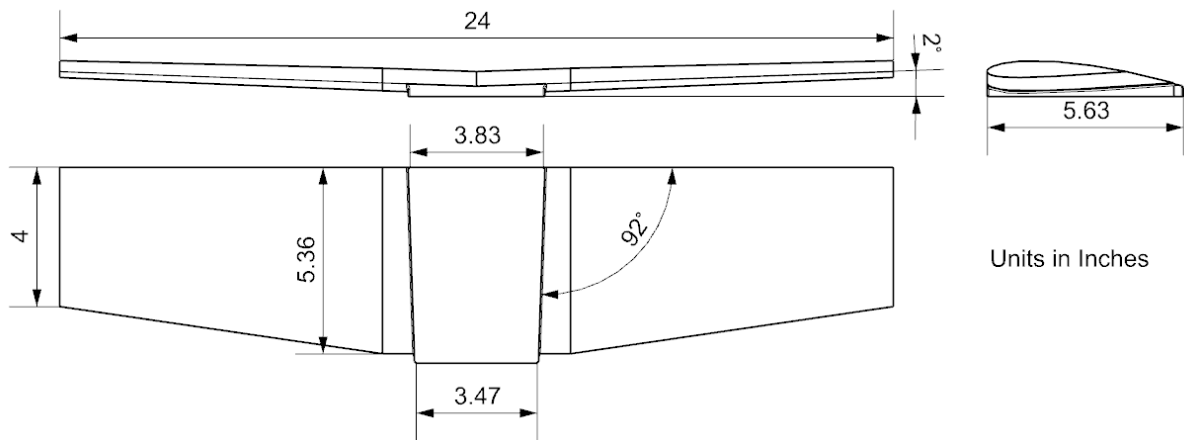Units in Inches

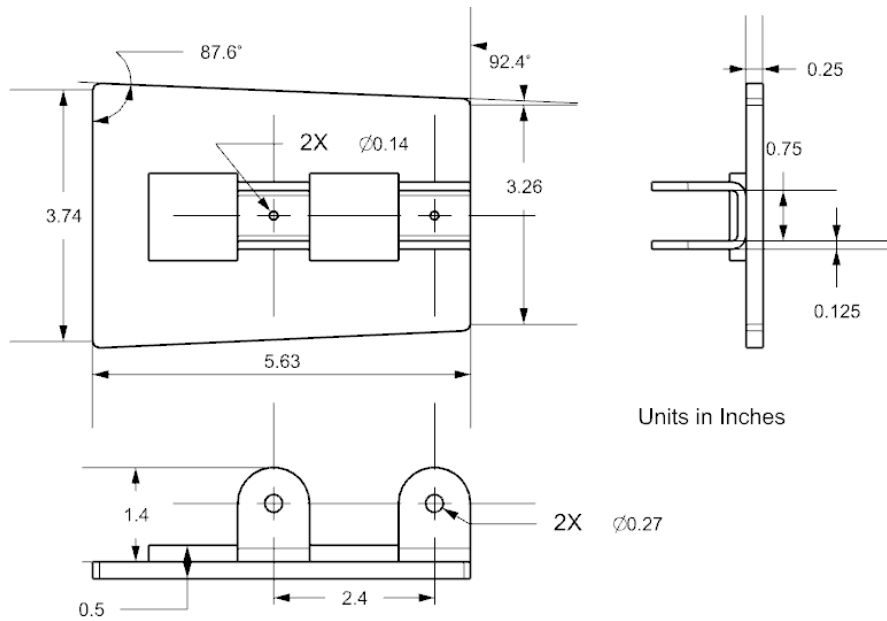**Figure A 4: Wake Rake Stand Dimensions**

Figure A 5: Wing Model Dimensions

Figure A 6: Wing Mount Attachment Dimensions